Cell

Clonal replacement sustains long-lived germinal centers primed by respiratory viruses

Graphical abstract

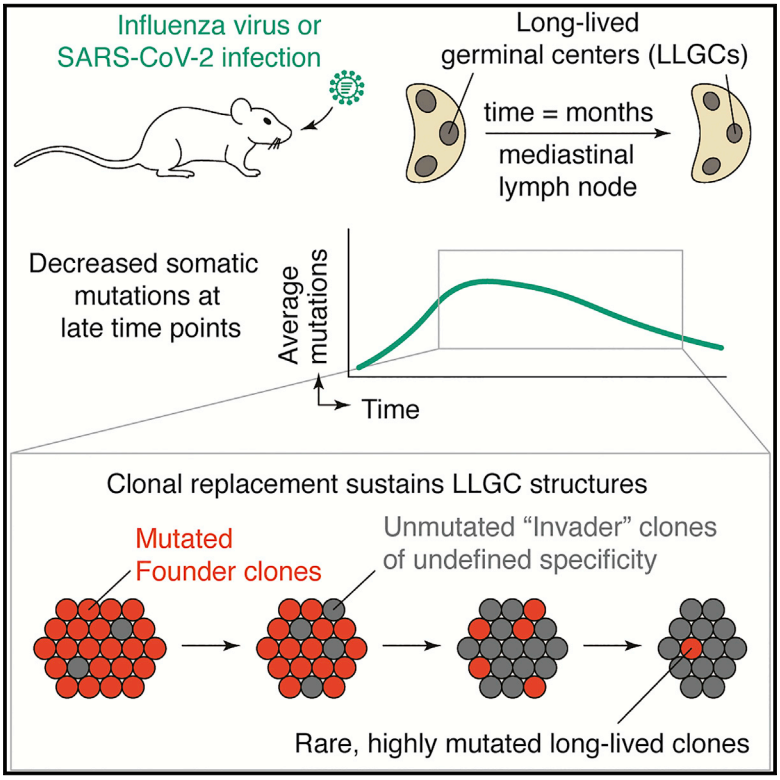

Highlights

- Influenza infection induces long-lived germinal centers (LLGCs)
- LLGCs are composed of "founder" and naive "invader" cells
- Invaders are not flu specific but compete with founders for affinity maturation
- Late founder clones export highly mutated memory cells that can be recalled

Authors

Renan V.H. de Carvalho, Jonatan Ersching, Alexandru Barbulescu, ..., Emily Yang, P.J. Utz, Gabriel D. Victora

Correspondence

victora@rockefeller.edu

In brief

B cells continue to hone their affinity for antigen in lymph-node germinal centers long after an initial respiratory virus infection, but as time goes on, new B cells that are less specific come to dominate the population. This work suggests that there are limits to how much a germinal-center reaction can hone the B cell and antibody repertoire over time.

de Carvalho et al., 2023, Cell *186*, 131–146
January 5, 2023
https://doi.org/10.1016/j.cell.2022.11.031

CellPress

Cell

CellPress

Article

Clonal replacement sustains long-lived germinal centers primed by respiratory viruses

Renan V.H. de Carvalho,[1,10] Jonatan Ersching,[1,10,11] Alexandru Barbulescu,[1,2,10] Alvaro Hobbs,[1] Tiago B.R. Castro,[1,3] Luka Mesin,[1] Johanne T. Jacobsen,[1] Brooke K. Phillips,[4] Hans-Heinrich Hoffmann,[5] Roham Parsa,[3] Maria Cecilia C. Canesso,[1,3] Carla R. Nowosad,[1,3] Allan Feng,[6,7] Sarah R. Leist,[8] Ralph S. Baric,[8,9] Emily Yang,[6,7] P.J. Utz,[6,7] and Gabriel D. Victora[1,12,*]

[1]Laboratory of Lymphocyte Dynamics, The Rockefeller University, New York, NY, USA
[2]Weill Cornell/Rockefeller/Sloan Kettering Tri-Institutional MD-PhD Program, New York, NY, USA
[3]Laboratory of Mucosal Immunology, The Rockefeller University, New York, NY, USA
[4]Rutgers Robert Wood Johnson Medical School and Princeton University MD/PhD Program, Piscataway, NJ, USA
[5]Laboratory of Virology and Infectious Disease, The Rockefeller University, New York, NY, USA
[6]Department of Medicine, Division of Immunology and Rheumatology, Stanford University School of Medicine, Stanford, CA, USA
[7]Institute for Immunity, Transplantation and Infection, Stanford University School of Medicine, Stanford, CA, USA
[8]Department of Epidemiology, University of North Carolina at Chapel Hill, Chapel Hill, NC 27599, USA
[9]Department of Microbiology and Immunology, University of North Carolina at Chapel Hill, Chapel Hill, NC 27599, USA
[10]These authors contributed equally
[11]In memoriam
[12]Lead contact
*Correspondence: victora@rockefeller.edu
https://doi.org/10.1016/j.cell.2022.11.031

SUMMARY

Germinal centers (GCs) form in secondary lymphoid organs in response to infection and immunization and are the source of affinity-matured B cells. The duration of GC reactions spans a wide range, and long-lasting GCs (LLGCs) are potentially a source of highly mutated B cells. We show that rather than consisting of continuously evolving B cell clones, LLGCs elicited by influenza virus or SARS-CoV-2 infection in mice are sustained by progressive replacement of founder clones by naive-derived invader B cells that do not detectably bind viral antigens. Rare founder clones that resist replacement for long periods are enriched in clones with heavily mutated immunoglobulins, including some with very high affinity for antigen, that can be recalled by boosting. Our findings reveal underappreciated aspects of the biology of LLGCs generated by respiratory virus infection and identify clonal replacement as a potential constraint on the development of highly mutated antibodies within these structures.

INTRODUCTION

Germinal centers (GCs) are the microanatomical site of affinity maturation, a Darwinian evolutionary process acting on B cells that ultimately results in the production of high-affinity antibodies to the driving antigen.[1–4] As such, GCs play a key role in the generation of humoral immunity to infection and vaccination. GC B cells undergo a cyclic process of somatic hypermutation (SHM) of immunoglobulin (*Ig*) genes followed by selection of mutants with improved affinity for antigen, which take place in the GC dark and light zones, respectively.[5,6] From this cyclic nature, it follows that the more time a B cell clone spends within a GC reaction, the greater the number of mutations it will accrue, and at least in theory, the higher the affinity it can ultimately achieve.[7] Extreme examples of this evolutionary process are the classic broadly neutralizing antibodies to HIV, which can replace up to 30% of variable-region amino acids by means of this process[8]—including substitutions that are highly improbable due to codon constraints or activation-induced cytidine deaminase (AID) mutational preferences[9,10]—thus acquiring extraordinary potency and cross-variant breadth. Achieving such high SHM load by immunization is a high priority for the field of HIV vaccination.[11]

Despite its importance, the factors that determine the duration of GC responses are poorly understood. GC reactions induced in mice by immunization with proteins in adjuvant persist from a few weeks to well over 1 month, depending on the antigen-adjuvant system used,[12,13] but do not normally allow formation of B cells with high SHM load.[14] On the other hand, GCs induced by certain acute viral infections, such as influenza, vesicular stomatitis virus, and likely SARS-CoV-2, can persist for several months.[15–19] The nature of these long-lasting GCs (LLGCs) and their consequences in terms of SHM and affinity maturation remain largely unexplored.[1,4,7] Better understanding of the biology of LLGCs would not only provide insight into general GC biology but may also pave

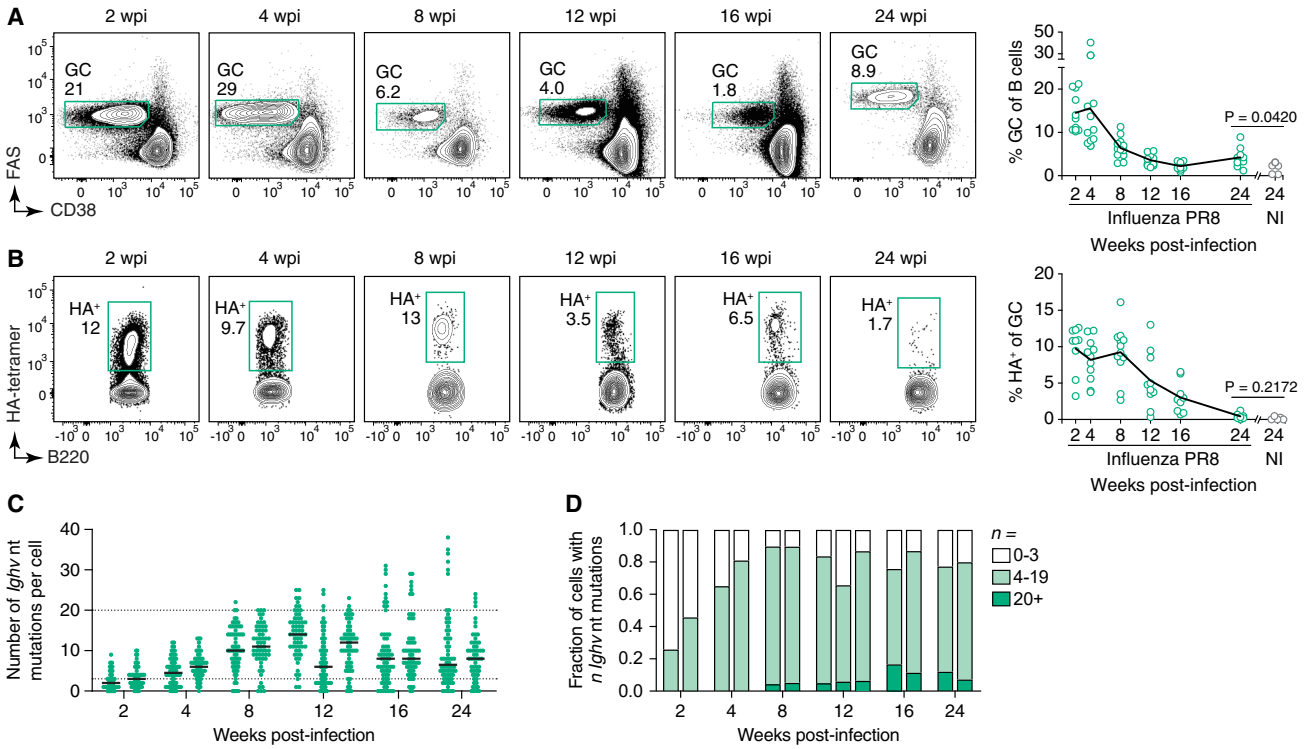

Figure 1. Kinetics and mutation profile of influenza-primed LLGCs up to 6 months after infection

(A and B) Representative flow cytometry plots showing frequency of GC B cells (FAS^+CD38^{low}) among total B cells ($B220^+$) and frequency of HA-binding B cells among all GC B cells in the mLN of wild-type C57BL/6 mice at different time points after influenza infection. Graphs on the right show pooled data from 3–4 independent experiments. Non-infected (NI) age-matched control mice assayed at the 24 wpi time point are shown for comparison. Each symbol is one mouse, and the line represents the mean.

(C and D) Somatic mutations in the *Igh* variable gene (*Ighv*) in single-sorted GC B cells at various time points post-infection, as in (A). In (C), each symbol represents one sequenced B cell (n = 55–74 cells/mouse), at least 2 mice per time point are shown (C). The same data are binned into cells with low, medium, and high SHM in (D).

See also Figure S1.

the way toward generating antibodies with long and complex SHM patterns by vaccination.

Here, we sought to investigate the properties and characteristics of the LLGCs triggered by acute viral infection in mice. We show that LLGCs primed by either influenza virus or SARS-CoV-2 are not maintained by long-lived B cell clones but rather persist as a result of constant replacement of virus-specific founder B cells by "naive"-derived invaders of undefined specificity. Nevertheless, rare founder B cells that persisted in GCs for 6 months or longer accumulated substantial SHM loads and developed high affinity for antigen, indicating that virus-primed LLGCs can be the source of highly mutated and potent antibodies despite pronounced clonal turnover.

RESULTS

Kinetics of formation and hypermutation in long-lasting influenza-primed GCs

To investigate the relationship between GC lifetime and SHM levels, we first determined the kinetics of GC formation and *Ig* hypermutation in the mediastinal lymph node (mLN) in response to influenza infection. We infected cohorts of wild-type C57BL/6J mice intranasally with 33 plaque forming units (p.f.u.) of mouse-adapted influenza A/Puerto Rico/8/1934 (PR8) virus and harvested mLNs at different time points up to 24 weeks post-infection (wpi). Large GCs were evident at 2 and 4 wpi, when GC-phenotype cells ($CD38^{low/-}Fas^{hi}$) accounted for an average of 15% of all B cells in the mLN (Figures 1A and S1). Following this peak, GC size decayed in two distinct phases. First, there was a rapid decline from 15% to 6.4% of GC B cells between 4 and 8 wpi. This decrease was followed by a period of relative stability, during which GC B cells fluctuated in frequency between 4.2% and 2.2% of all B cells, consistently higher than the background of GC B cells in the mLN of uninfected co-housed littermates (Figure 1A) and in line with previous publications using similar influenza models.[16,19] Staining with $H1_{PR8}$ tetramers showed that the proportion of GC B cells that bound HA, although highly variable, tended to decrease with time. Still, HA-binding B cells were observable in some mice as late as 24 wpi (Figure 1B).

To determine whether these LLGCs are an abundant source of B cells with high SHM load, we sequenced the *Igh* genes of single B cells sorted from mLN GCs at several time points after influenza

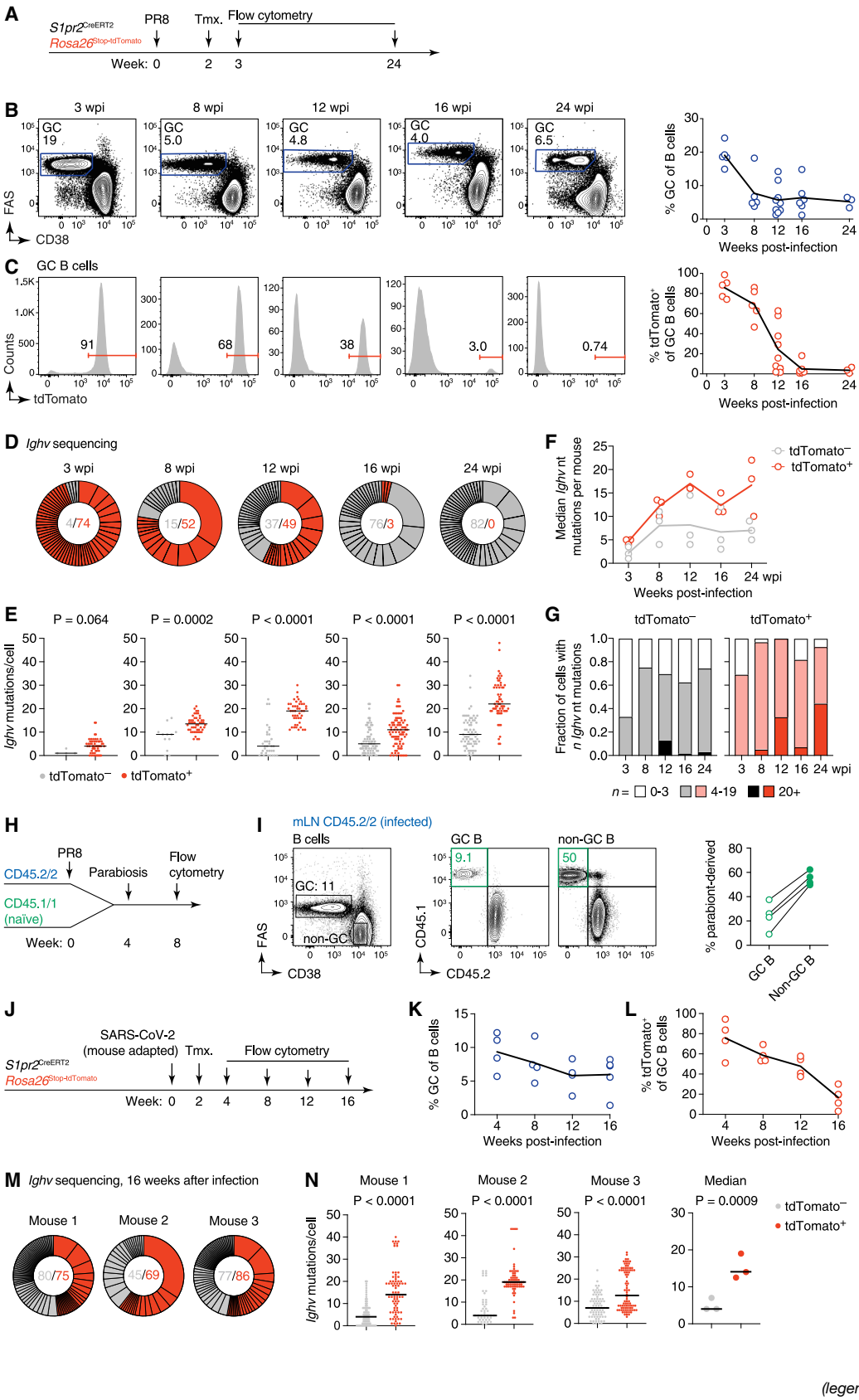

(legend on next page)

infection. As expected, the median number of nucleotide (nt) mutations per *Ighv* segment increased from 2 nt at 2 wpi to 11 nt at 12 wpi. However, rather than continuing to increase, median SHM began to drop at 12 wpi, falling to 8 nt at both 16 and 24 wpi (Figure 1C). Accordingly, the proportion of cells carrying 0–3 *Ighv* nt mutations decreased from 70% at 2 wpi to 10% at 8 wpi, after which it climbed again to 22% at 24 wpi. Highly mutated cells (defined as carrying >20 *Ighv* nt mutations) initially increased with time, peaking at 14% at 16 wpi, after which they also decreased (Figure 1D). Therefore, rather than increasing monotonically, the degree of SHM in influenza-primed LLGCs peaks and then decreases as the GC progresses.

LLGCs are sustained by turnover of B cell clones within a persistent GC B cell population

A likely explanation for the failure of LLGCs to accumulate somatic mutations monotonically is that the founder clones present in early and peak GCs are gradually replaced by incoming B cells that are unmutated. To verify this, we fate-mapped B cells at the GC peak in S1pr2-CreERT2 x *Rosa26*$^{\text{Lox-Stop-Lox-tdTomato}}$ (S1pr2-Tomato) mice (Figure 2A), which allow highly efficient fate-mapping of GC B cells.[20] A single dose of tamoxifen administered at day 14 post-infection resulted in labeling of on average 86% of mLN GC B cells a week later (Figures 2B and 2C). The proportion of fate-mapped B cells remained high in GCs throughout the initial decay phase (between 4 and 8 wpi) but fell sharply between 8 and 16 wpi. Although kinetics varied between mice, founders accounted for a uniformly low fraction of all GC B cells at 16 and 24 weeks (Figures 2B and 2C). Thus, late-stage influenza-induced mLN GCs are largely devoid of the B cell clones that seeded these reactions.

Igh sequencing (Figures 2D–2G and S2A) showed that SHM load increased more reliably with time in the fate-mapped population (Figures 2E, 2F, and S2A), so that B cells with few (0–3) *Ighv* nt mutations became progressively depleted as highly mutated cells (≥20 *Ighv* nt mutations) accumulated (Figure 2G). By contrast, non-fate-mapped cells were significantly less mutated (Figure 2E) and included a substantial contingent of cells with 0–3 *Ighv* nt mutations even at the latest time point (Figure 2G). Despite the overall lower mutation frequency among non-fate-mapped clones, somatic mutations still accumulated over time in this population (Figures 2E, 2G, and S2A), consistent with at least some of these clones becoming long-term participants in the ongoing GC.

To define the origin of non-fate-mapped B cells in LLGCs and to rule out that replacement of fate-mapped cells was due to either lower fitness or immune rejection of cells expressing the non-self tdTomato protein, we carried out analogous experiments using parabiosis. Wild-type mice were infected with PR8 influenza virus, joined parabiotically to mice carrying a different allele of CD45, and assayed 4 weeks after surgery (Figure 2H). Seeding of ongoing GCs by B cells derived from the uninfected parabiont was evident at this time point, with an average GC chimerism of 24%, compared with 55% in non-GC B cells (Figure 2I), supporting a naive origin for the incoming B cell clones. Similar analysis of Tfh cells showed that this population is replaced at an even higher rate than GC B cells are (Figures S3A–S3C), consistent with our previous observation that GCs are permissive to exchange and replacement of Tfh cell clones.[21]

To determine whether clonal replacement in LLGCs is general feature of respiratory tract infections, we infected S1pr2-Tomato mice with mouse-adapted SARS-CoV-2,[22] fate-mapping GC B cells at 2 wpi (Figure 2J). SARS-CoV-2-infected mice showed abundant GCs in the mLN that did not decay substantially over the 16-week follow-up (Figures 2K and S2B). Nevertheless, as

Figure 2. Replacement of founder clones over time in influenza-primed LLGCs

(A) Experimental setup.

(B and C) Representative flow cytometry plots showing frequency of GC B cells (FAS^{+}CD38^{low}) among total B cells (B220^{+}) (B) and frequency of fate-mapped B cells among all GC B cells (C) in the mLN of tamoxifen-pulsed S1pr2-Tomato mice at different time points after influenza infection. Graphs on the right show pooled data from 2 to 5 independent experiments. Each symbol is one mouse, and the line represents the mean.

(D) Representative charts showing distribution of tdTomato^{+} founder (red) and tdTomato^{-} invader (gray) B cells sorted from GCs at different time points after influenza infection. Each slice represents one clone (defined as B cells with the same *Igh* VDJ rearrangement). Gray and red numbers in the center of the pie charts denote how many invader and founder GC B cells were sequenced, respectively, when GC B cell samples were sorted in an unbiased manner (thus, the zero fate-mapped cells in the 24 wpi pie chart). Each chart is from one mouse; additional charts shown in Figure S2.

(E) Numbers of nucleotide mutations in *Ighv* among the cells shown in (D). Each symbol represents one sequenced B cell (n = 55–74 cells/mouse). Additional plates of rare fate-mapped GC B cells were sorted for the late time points (16 and 24 wpi). p values are for Mann-Whitney U test.

(F) Median SHM per mouse for combined data from (E) and from additional mice shown in Figure S2A.

(G) Same data as in (F), binned into cells with low, medium, and high SHM.

(H) Experimental setup. A C57BL/6 (CD45.2) mouse was infected with influenza and joined parabiotically to a naive B6.SJL mouse (CD45.1) at 4 wpi.

(I) Representative flow cytometry plots showing the participation of CD45.2 founder and CD45.1 invader cells in mLN GCs of the infected CD45.2 parabiont at 8 wpi. Non-GC B cells are shown for comparison. Graph on the right summarizes data for 4 parabiosis pairs. Either the CD45.2 or CD45.1 partners were infected in different experiments.

(J) Experimental setup as in (A). S1pr2-Tomato mice are infected with mouse-adapted SARS-CoV-2, GC B cells are fate-mapped at 2 wpi, and GC composition is followed by flow cytometry at different time points.

(K and L) Graphical representation of the kinetics of total GC B cells (K) and fate-mapped GC B cells over time (4–16 weeks), after infection with SARS-CoV-2. The results are pooled from 2 independent experiments. Each symbol is one mouse, and the line represents the mean.

(M) Pie charts showing distribution of tdTomato^{+} founder (red) and tdTomato^{-} invader (gray) B cells sorted from GCs at 16 weeks after SARS-CoV-2 infection. Each slice represents one clone (defined as B cells with the same *Igh* VDJ rearrangement). Gray and red numbers in the center of the pie charts denote how many invader and founder cells were sequenced, respectively. Each plot is from one mouse.

(N) Number of nucleotide mutations in *Ighv* among the cells shown in (M). Each symbol represents one sequenced B cell. Median SHM per mouse is shown on the right. p values are for Mann-Whitney U test.

See also Figures S2 and S3.

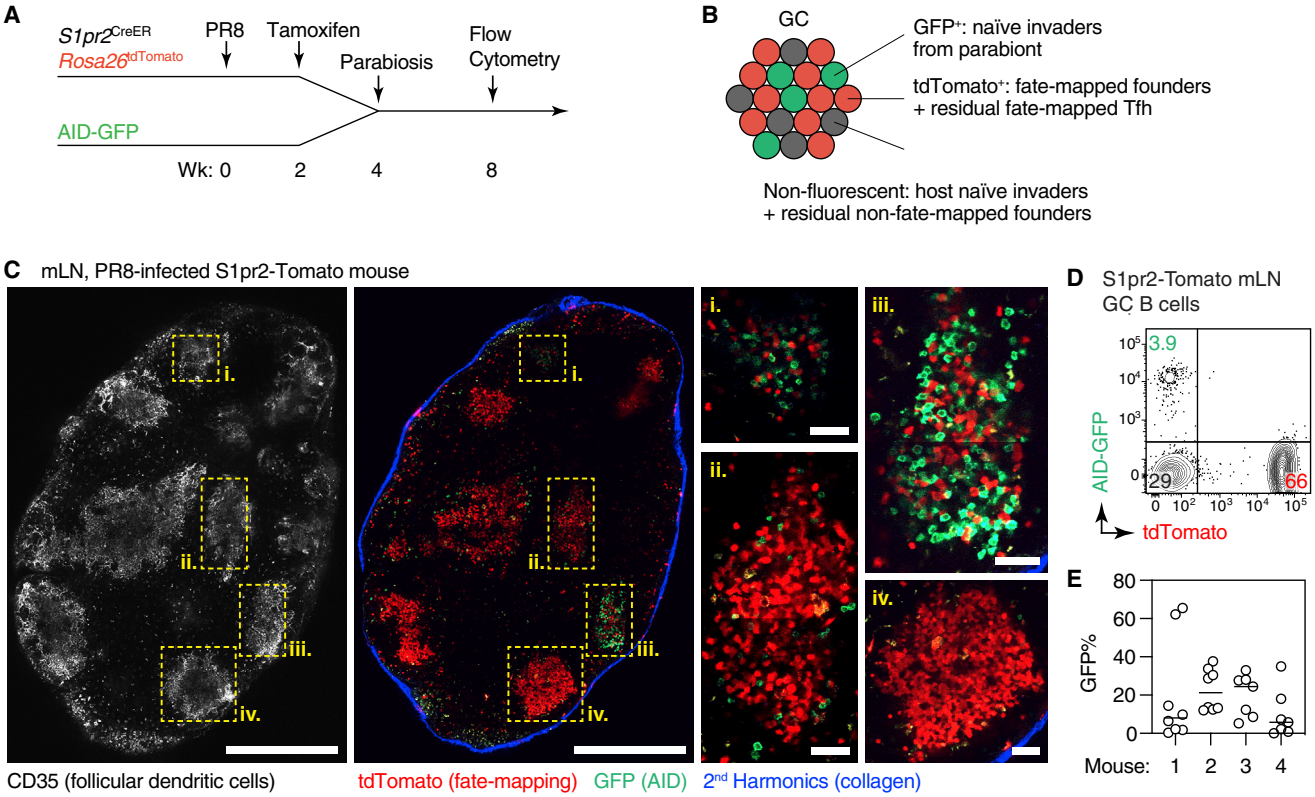

Figure 3. Clonal replacement results from invasion of ongoing GCs by naive-derived B cells

(A) Experimental setup.

(B) Cellular composition of invaded GCs.

(C) Multiphoton imaging of an infected mLN (collapsed 3-slice, 40 μm z stack), highlighting GCs with different degrees of invasion by parabiont-derived B cells (i., ii., iii., and iv.). GCs are defined based on follicular dendritic cell networks, stained *in vivo* by administration of a monoclonal antibody to CD35 (leftmost panel).

(D) Representative flow cytometry plot showing the identification of parabiont-derived invader cells (AID-GFP) in whole mLN.

(E) Frequency of AID-GFP$^+$ invaders among individual GCs, determined by imaging. Each symbol represents the ratio of GFP$^+$ over tdTomato$^+$ cells in one individual GC. Each column shows all of GCs analyzed in 4 individual mice from 4 independent experiments.

with influenza virus, the percentage of fate-mapped B cells in SARS-CoV-2 GCs decreased with time, from 76% at 4 wpi to 17% at 16 wpi (Figures 2L and S2C), indicative of clonal replacement also in this system. Sequencing of tdTomato$^+$ (founder) and tdTomato$^-$ (invader) GC B cells at 16 wpi showed that SHM loads among founder B cells were on average 3 times those of invader cells (Figures 2M and 2N), again in line with what was seen for influenza-induced GCs. Thus, clonal replacement is not an exclusive feature of influenza and may represent a common feature of late-stage GCs, especially those primed by respiratory viral infection.

We conclude that in LLGCs induced by both influenza and SARS-CoV-2 infection, mean SHM load does not increase indefinitely with time due to progressive replacement of founder clones by incoming naive-derived B cells.

Clonal replacement results from invasion of ongoing GC structures

Although our fate-mapping and parabiosis showed that incoming naive B cells contribute substantially to LLGCs at the population level, they did not distinguish between *de novo* establishment of new GC structures in empty follicular dendritic cell (FDC) niches and true invasion of ongoing GCs, as achieved under controlled conditions in hapten-carrier immunization systems.[7,23,24] To make such a distinction, we infected S1pr2-Tomato mice with PR8 influenza virus, which we fate-mapped with tamoxifen at 2 wpi and then joined parabiotically to uninfected AID-GFP mice at 4 wpi (Figure 3A). In this setup, tdTomato$^+$ cells are founder B cells (plus a negligible fraction of fate-mapped Tfh cells, given the low efficiency of S1pr2-Tomato in fate-mapping this population), and GFP$^+$ cells represent the roughly one-half of invaders derived from the parabiont. Non-fluorescent GC B cells include the other half of invaders coming from the S1pr2-Tomato host itself, plus a minor fraction of non-labeled founders (Figure 3B). We imaged intact explanted mLNs of infected S1pr2-Tomato partners by two-photon microscopy at 8 wpi (Figure 3C), when the full GC population contained an average of 4% GFP$^+$ invader B cells, as measured by flow cytometry (Figure 3D). mLN imaging revealed that GCs that contained GFP$^+$ B cells also consistently contained fate-mapped S1pr2-Tomato cells, whereas we observed no instances of GCs containing only GFP$^+$ B cells among their

Figure 4. Clonal and transcriptional characteristics of founder and invader B cells

(A and B) Experimental setup.

(C) Representative images of founder- and invader-dominated GCs, estimated from frequency of fate-mapped CD45.2$^+$tdTomato$^+$ B cells (red).

(D) Clonal distribution of founder (orange) and invader (green) clones in sorted GCs. CD45.2$^+$tdTomato$^-$ cells (hatched) were not sequenced. The size of the orange, green, and hatched sectors of the chart was determined by flow cytometry. Internal slices are based on *Igh* sequencing. 6 GCs from 2 parabiosis pairs were analyzed.

(E) Clonal diversity (D50, or the fraction of clones accounting for 50% of cells sequenced) plotted against the degree of invasion for founder (left) and invader (right) clones. Each symbol represents one GC. p values are for Spearman correlation.

(F) D50 and fraction of small clones (accounting for <10% of sequenced cells in that population) among founder and invader cells. Each symbol represents one GC. p values are for Mann-Whitney U test.

(G) Number of nucleotide mutations in *Ighv* among founder and invader B cells in each GC. Each symbol represents one sequenced cell. $p_{Mann\text{-}Whitney} < 0.0001$ for all comparisons of invaders versus founders within the same GC.

(H) Clonal phylogenies of expanded clones from one founder and 3 invader-dominated GCs. Colors and roman numerals correspond to those in (D).

(legend continued on next page)

fluorescent population at this time point (Figure 3E). Thus, incoming B cells join GCs that are already occupied by founder B cell clones, rather than starting their own GC structures *de novo*. Individual GCs were invaded by naive B cells at widely disparate rates, even within the same LN. For example, in the mLN from mouse 1 (Figure 3E), whereas most GCs contained relatively few invaders (0–20 per 100 tdTomato$^+$ B cells), two GCs were heavily invaded, containing roughly equal numbers of GFP$^+$ invaders and tdTomato$^+$ founders. Such variation was also observed in three other imaged lymph nodes from independent mice (Figure 3E). Thus, the clonal replacement observed in late influenza-induced GCs results from invasion of ongoing GCs by naive-derived B cells. We conclude that the prolonged GC reactions observed following influenza infection in mice therefore consist of long-lived GC structures that house predominantly shorter-lived B cell clones that progressively turn over with time.

GC invasion is polyclonal and is expanded by positive selection of invader clones

To investigate the factors responsible for the different degrees of invasion seen in individual GCs, we combined parabiosis with *in situ* photoactivation,[6] which allows us to obtain strictly defined populations of founder and invader B cells from the same GC. We infected with PR8 S1pr2-Tomato mice carrying a PAGFP-transgene, fate-mapped these mice at 2 wpi, then parabiotically joined them to naive PAGFP-transgenic mice carrying the CD45.1 congenic allele 2 weeks later. mLNs were harvested 4 weeks after parabiosis for analysis (Figure 4A). Invaded GCs in the infected parabiont contained three populations: parabiont-derived tdTomato$^-$CD45.1$^+$ invaders, host-derived tdTomato$^+$CD45.2$^+$ founders, and host-derived tdTomato$^-$ CD45.2$^+$ B cells, composed of invaders as well as any founder clones that failed to become fate-mapped in response to tamoxifen (Figure 4B). From each mLN, we photoactivated individual GCs with low or high invader content (estimated from images based on the density of tdTomato$^+$ cells in each GC), dissected LN into fragments containing a single photoactivated GC, and then sorted photoactivated tdTomato$^+$ founder and CD45.1$^+$ invaders from each fragment (Figure 4B).

We obtained cells from 6 GCs, ranging from 1.3% to 79% of tdTomato$^-$ invader B cells as determined by flow cytometry (Figure 4C). Invading B cells were clonally diverse even in the least invaded GCs. For example, the 31 cells sequenced from the 1.3% CD45.1$^+$ invader population of the least invaded GC (GC1) were composed of 23 different clones, most identified only once (Figure 4D). This suggests that GC invasion is relatively common, rather than being reserved for rare naive B cells with high affinity for the viral antigen. Pronounced invasion was associated with emergence of larger invader-derived clones (Figure 4D): all three GCs containing ~30% or fewer founder B cells (GC3, 4, and 6) included invader clones that represented >15% of all cells in that GC (Figures 4E and 4F). Regardless of the degree of invasion, invaders always carried fewer somatic mutations than founders (means per GC ranging from 1.7 to 4.8 nt among invaders and 11.1 to 17.8 nt among founders) (Figure 4G). Clonal trees drawn from expanded clones (Figure 4H) showed frequent large clonal expansions ("clonal bursts"[25]) at several points in both founder and invader clones, suggestive of active positive selection among both populations (Figure 4H). Thus, clonal replacement is the result of active competition between founders and invaders within the same GC structure.

To verify this at the transcriptional level, we performed single-cell RNA sequencing (scRNA-seq) on samples of invader and founder clones (fate-mapped as in Figure 2A) obtained from GCs at 8 wpi, as well as on 3 wpi controls. B cells segregated transcriptionally into the typical clusters defined by GC zoning, cell cycle, and selection for cyclic re-entry or export (Figures 4I and 4J; see Figures S4A–S4D for a full description). *Ig* gene analysis revealed the expected decrease in clonal diversity with time among founder clones. However, invader clones at 8 wpi were as diverse as founder clones at 3 wpi, as expected if GC invasion is polyclonal (Figure 4K). Cells from the three experimental groups were evenly distributed in transcriptional space, with the exception of clusters 0 and 1 (assigned to G1-phase cells in the dark and light zones, respectively), where segregation was evident between B cells from the 3 and 8 wpi time points, but not between tdTomato$^+$ founder and tdTomato$^-$ invader cells from the 8 wpi cohort. Distribution of 8 wpi founders and invaders across 8 of the 9 clusters was statistically indistinguishable, including in clusters associated with positive selection, such as cluster 6 (*Myc*), 7 (*PB*), and 8 (*pre-MBC*). tdTomato$^+$ cells were significantly enriched in cluster 4 (*G2/M*), possibly due to slightly increased proliferative capacity among founders (Figure 4L). The similarity between invaders and founders was confirmed by differential gene expression, which revealed few significant changes between tdTomato$^+$ and tdTomato$^-$ cells (Figures 4M and S4E). Notably, one of the genes upregulated in tdTomato$^+$ B cells was *Ccnd3*, encoding for cyclin D3, a key driver of the "inertial" mode of GC proliferation that drives clonal bursting,[26,27] again indicating that tdTomato$^+$ founder B cells are actively undergoing positive selection during the invasion period.

We conclude that clonal replacement is the result of polyclonal invasion of GCs in which founder clones are still actively undergoing positive selection. Once invader clones enter a GC, they closely resemble founders, both transcriptionally and in their ability to undergo positive selection for clonal expansion and post-GC differentiation. The observation that invasion progresses even in face of the slightly higher proliferative capacity of founder clones suggests that clonal replacement involves a combination of constant invasion by new B cells and positive selection of assimilated invaders.

(I–M) scRNA-seq of GC B cells derived from infected mLNs of S1pr2-Tomato mice treated as in Figure 2A, sorted at 3 (tdTomato$^+$ cells only) or 8 (tdTomato$^+$ and tdTomato$^-$) wpi. Uniform manifold approximation and projection (UMAP) plots showing distribution of sequenced B cells colored by transcriptionally defined cluster (I) or by time point/origin (J). (K) Distribution of clones according to size and time point/origin (L) Percentage of tdTomato$^+$ founder B cells in each transcriptional cluster (as defined in I). Includes only cells 8 wpi. (M) Genes differentially expressed between tdTomato$^+$ founder and tdTomato$^-$ invader B cells (left) or between 3 and 8 wpi time points (right). The number of differentially expressed genes is indicated above each plot.

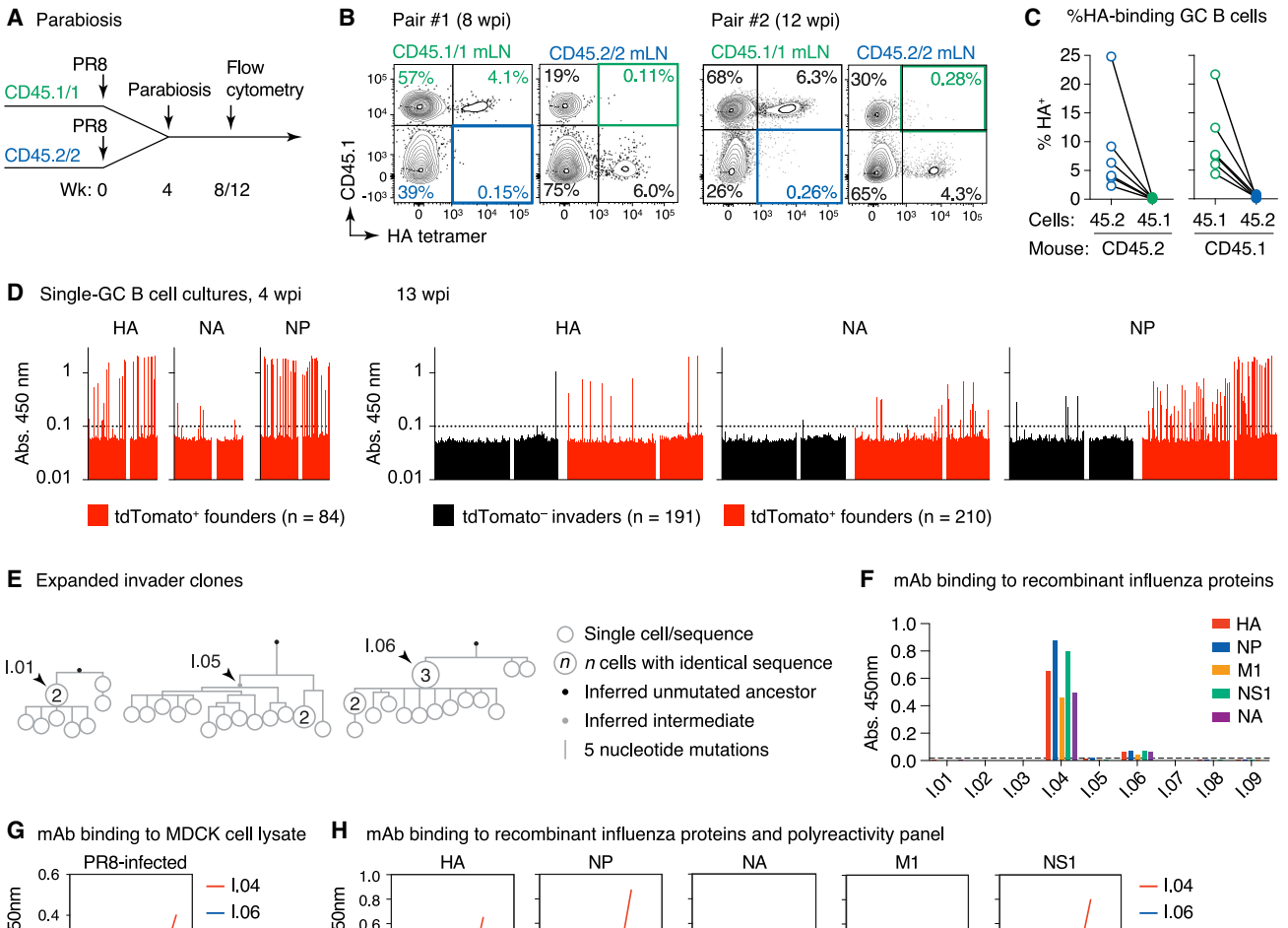

(legend on next page)

B cell clones that invade long-lived GCs do not detectably bind influenza antigens

Previous studies have shown that invasion of ongoing GCs by B cells of the same antigenic specificity requires that invaders have higher affinity for antigen than the founders.[24] This is unlikely to be the case in our system given that at the time of invasion, founders have previously undergone substantial affinity maturation. Alternatively, ongoing GC cells can be invaded by incoming B cells with specificities other than those recognized by the founder clones,[23] irrespective of their affinity.

To distinguish between these possibilities, we performed parabiosis on allelically distinct pairs of PR8-infected mice (wild-type C57BL/6, and SJL) and measured HA specificity among invader populations at 8 or 12 wpi by flow cytometry using HA tetramers. In both instances, substantial binding to HA was detectable only in the founder but not the invader population (Figures 5A–5C). This was also the case when only one of the parabionts was infected (Figures S5A–S5C), ruling out that infrequent HA binding among invaders was due to depletion of the HA-specific naive repertoire in the infected mouse in this setting. Likewise, when S1pr2-Tomato mice were infected with SARS-CoV-2, binding to spike protein was largely restricted to fate-mapped founder cells at 8 wpi (Figures S5D and S5E). To determine whether the same properties were true also for other influenza antigens, we used single-GC B cell cultures[28] to assay the antibodies produced by founders and invaders against multiple proteins. We sorted founder and invader GC B cells from infected and fate-mapped S1pr2-Tomato mice into 96-well plates containing NB-21.2D9 feeder cells[28] at 13 wpi (Figure 5D), plus 4-wpi founder populations as positive controls. We then measured reactivity to three major influenza virus antigens—HA, neuraminidase (NA) and nucleoprotein (NP)[29]—for all cultures yielding detectable levels of IgG. Influenza-reactive supernatants were frequent among tdTomato$^+$ founder-derived cultures both at 4 and 13 wpi (accounting for 71% and 46% of IgG$^+$ wells, respectively). By contrast, far fewer (3.7%) of the tdTomato$^-$ supernatants assayed bound detectably to these antigens (Figure 5D), in agreement with the near absence of HA-binding cells from the invader population in flow cytometry (Figures 5B and 5C). The remaining tdTomato$^-$ binders could in principle represent founder cells that failed to recombine the *Rosa26*^{tdTomato} allele in response to tamoxifen. To test for this, we coupled fate-mapping with parabiosis to assay the specificity of invader B cells strictly defined as arising from the naive parabiont (Figure S5F). Although binding to influenza antigens was detectable in 59% of tdTomato$^+$ founder cells at 13 wpi, it was completely absent from the parabiont-derived (tdTomato$^-$ CD45.1$^+$) invader population at this time point (Figure S5G).

To rule out that the failure of invader B cell antibodies to bind influenza was due to their early stage of affinity maturation, we measured the reactivity of mAbs cloned specifically from invader GC B cells showing strong evidence of positive selection at later time points after infection. Using *Ig* sequences obtained from invader GC B cells sorted from the S1pr2-Tomato mice shown in Figure 2D, we built phylogenetic trees for the most expanded B cell clones found at different time points post-infection (Figure 5E), from which we generated 9 mAbs corresponding to key clonal expansion points in the phylogeny (3, 1, and 5 mAbs from 12, 16, and 24 wpi, respectively; Figure 5E). Despite originating from sequences likely to have undergone positive selection, 7 of 9 invader-derived antibodies failed to bind to any of five influenza antigens tested (HA, NA, NP, M1, and NS1) (Figure 5F) or lysates of Madin-Darby canine kidney (MDCK) cells infected with PR8 virus, as assayed by ELISA (Figure 5G). These clones also failed to bind HA and NP in a highly sensitive biolayer interferometry (BLI) avidity-based assay in which Fabs are immobilized on the sensor and then probed for binding to tetramerized antigens (Figure S5H), an assay previously shown to enable detection of very low affinity binding events.[30] Two invader-derived antibodies (I.04 and I.06), taken from a clonal burst with only few *Ighv* mutations cloned from 24 and 12 wpi, respectively, showed reactivity at high concentrations to all influenza proteins tested, as well as to PR8-infected MDCK lysates (Figures 5F–5H). These antibodies also bound to non-infected MDCK lysates and to antigens in the classic polyreactivity panel (Figures 5G and 5H) and were thus classified as polyreactive rather than influenza-specific. Further assaying of non-polyreactive invader-derived antibodies for binding to a panel of common autoantigens[31] and fecal bacteria (as a representative of the immunostimulatory antigens present in the cage environment) failed to reveal consistent binding patterns among invader-derived antibodies (Figures S5I and S5J). Taken together, our

Figure 5. Invader B cells are not specific for influenza antigens

(A) Experimental setup.

(B) Representative flow cytometry plots showing the frequency of endogenous and parabiont-derived GC B cells that bind HA in mLNs of both mice at 8 (left) and 12 (right) wpi.

(C) Quantification of data as in (B).

(D) Binding of founder (tdTomato$^+$) and invader (tdTomato$^-$) GC B cells to influenza HA, NA, and NP antigens at 4 or 13 wpi. GC B cells were sorted from mLNs of S1pr2-Tomato mice into 96-well plates for single-cell (Nojima) culture, and IgG$^+$ supernatants were assayed against influenza antigens by ELISA. Each bar represents one IgG$^+$ culture. Data are pooled from two mice.

(E–H) *Igs* of expanded invader clones were sequenced and their encoded mAbs were produced for binding assays. (E) Phylogeny inferences based on *Ighv* sequences for 3 selected clones. The arrowhead indicates the produced mAb. (F) Binding to different influenza antigens was assayed for 9 such mAbs at 100 nM. (G and H) mAbs were titrated and incubated in the presence of PR8-infected cell lysate, uninfected cell lysate (negative control) (G), and panels of influenza (HA, NA, NP, M1, and NS1) and polyreactivity (dsDNA, ssDNA, insulin, keyhole limpet hemocyanin [KLH], and lipopolysaccharide – LPS) antigens (H). For polyreactivity assays, mAbs ED38 and MG053 were included as positive and negative controls, respectively.

(I) Experimental setup.

(J) Flow cytometry plots showing absence of invasion by mutant (CD45.2) B cells in the mLN of the infected CD45.1 mouse. Data from multiple mice are quantified to the right of each flow cytometry plot.

Data representative of at least three independent experiments on biological replicates (at least 2 parabiotic pairs per experiment).

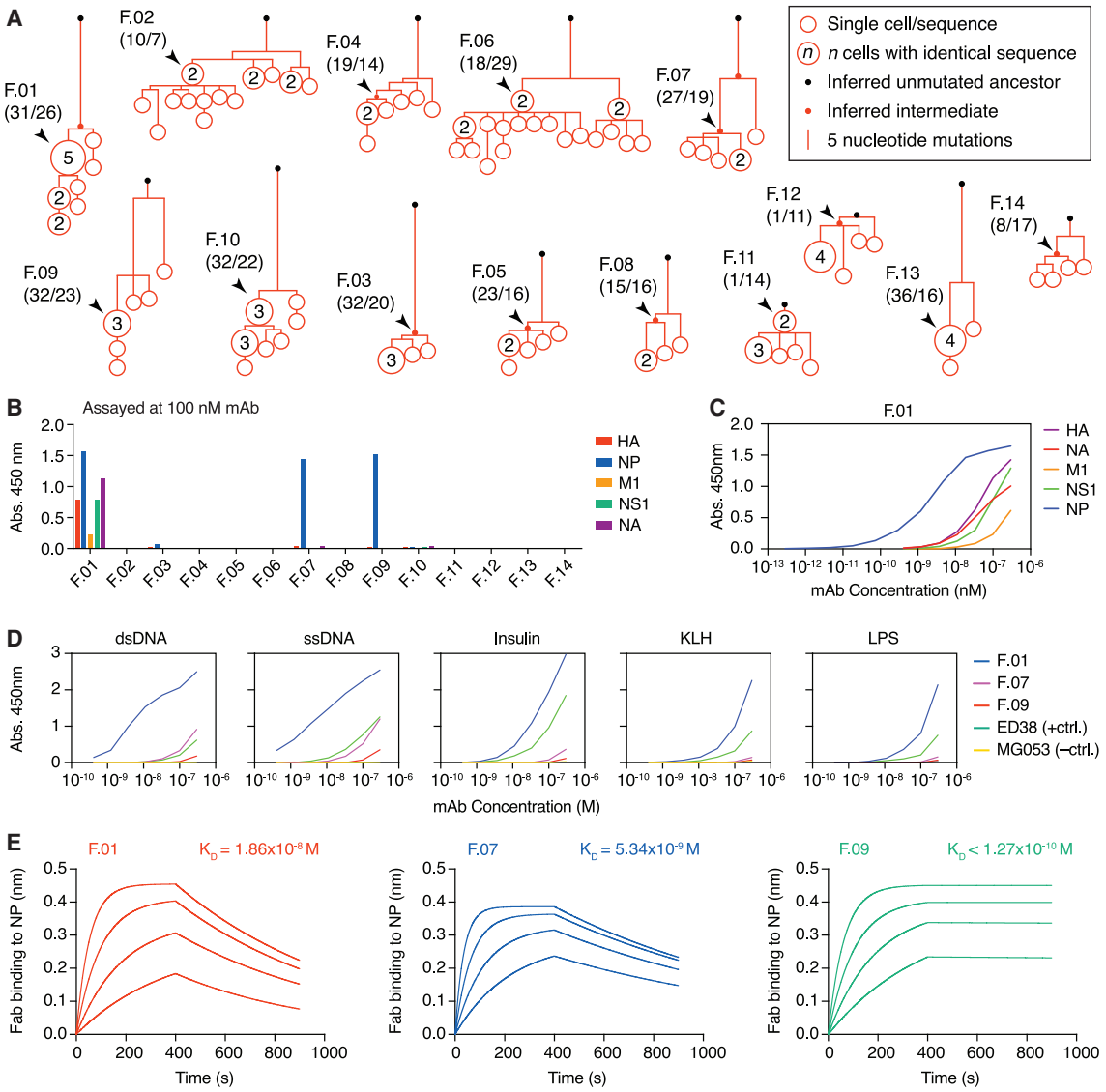

Figure 6. Binding properties of long-lasting founder B cells

(A) Phylogeny inferences based on *Ighv* sequences of 14 selected founder clones present in the mediastinal GC 24 weeks post infection.

(B) mAbs derived from founder clones were assayed for binding to recombinant PR8 influenza proteins by ELISA. Shown are the Abs. 450 nm values for each mAb assayed at 100 nM.

(C) ELISA titration curves for mAb F.01 binding to recombinant influenza proteins.

(D) ELISA titration curves for mAbs F.01, F.07, and F.09 binding to antigens of the polyreactivity panel. mAbs ED38 and MG053 were included as positive and negative controls, respectively.

(E) Bio-layer interferometry for Fabs F.01, F.07, and F.09 binding to NP, assayed at concentrations of 20, 40, 80, and 160 nM of Fab. Affinities are average of four measurements fitted globally at 20–160 nM range. The off rate of Fab F.09 was below the detection limit of the assay.

Results are medians of technical triplicates and are representative of two independent experiments (B–D).

reactivity data suggest that invader clones are most likely specific for antigens other than those of influenza, although we cannot exclude extremely low affinity binding or specificity toward cryptic forms of influenza antigens not detectable using recombinant proteins.[28]

To rule out that GC invasion results from stochastic recruitment of B cells, regardless of their specificity, we parabiotically joined influenza-infected wild-type mice with either one of two strains of mice with restricted or no B cell receptor (BCR) specificity. First, we used the MD-4 strain (Figures 5I and 5J), in which >95% of cells express a BCR specific for hen egg lysozyme (HEL).[32] Second, we used D_H-latent membrane protein 2A (LMP2A) mice (Figures 5I and 5J), in which the *Igh* D segments are replaced by latent membrane protein 2A (LMP2A) of Epstein-Barr virus, mimicking downstream BCR signals. Although these mice lack BCR expression, B cells expressing

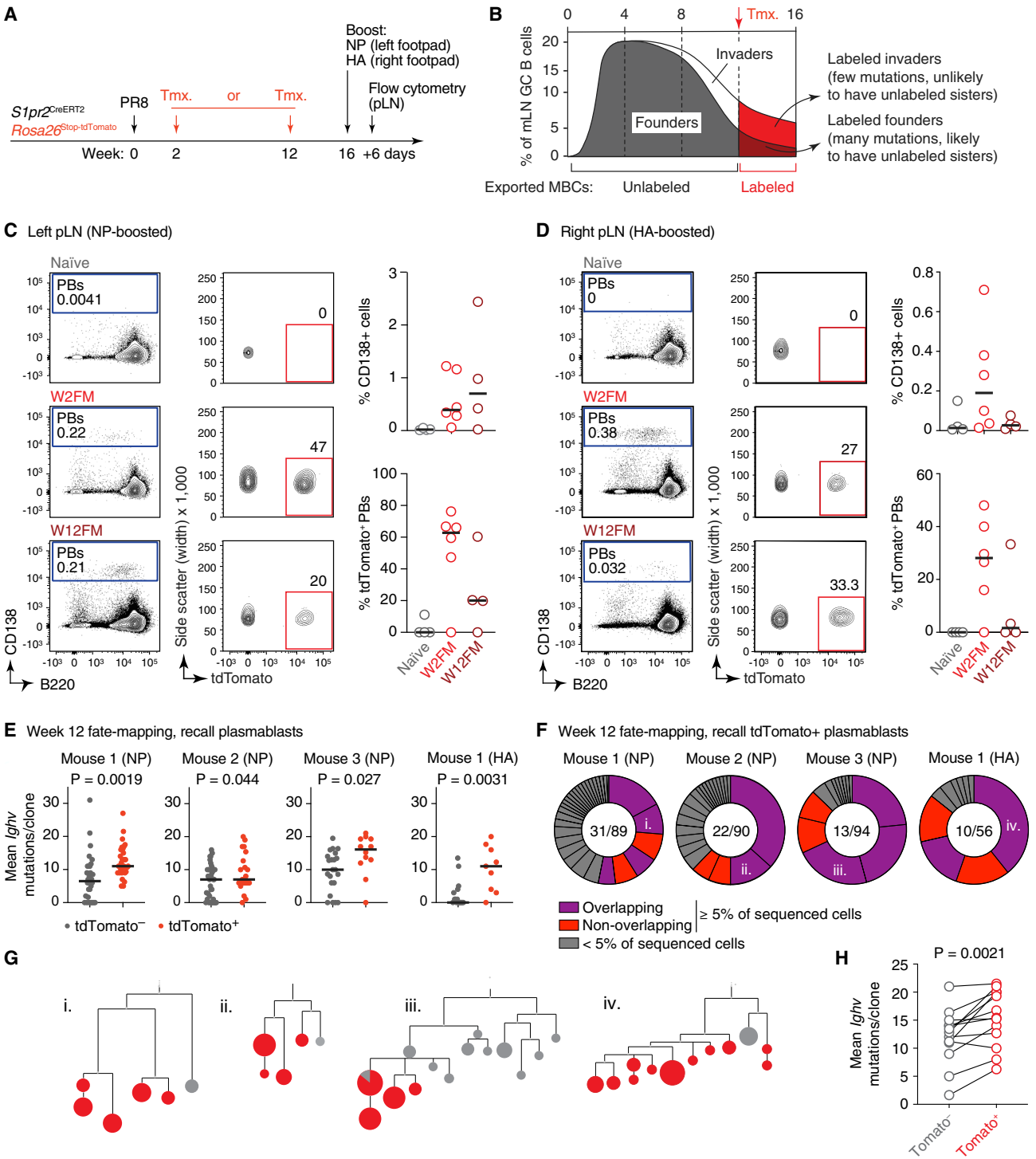

Figure 7. Late founder-derived memory B cells from LLGCs contribute to recall responses

(A) Experimental setup.

(B) Expected abundance and sequence-level phenotypes of founder and invader GC B cells labeled by tamoxifen treatment at 12 wpi. MBCs, memory B cells.

(C and D) Representative flow cytometry plots showing frequency of total PBs (CD138^{hi}, gated on total TCR-β^{-} LN cells) and fate-mapped PBs (tdTomato^{+}, gated on CD138^{hi} cells) in pLNs boosted with NP (C) or HA (D) in PR8-infected mice pulsed with tamoxifen at early (W2FM) or late (W12FM) time points after infection, compared with age-matched non-infected controls fate mapped at the late time point. Graphs on the right show pooled data from 2 independent experiments. Each symbol is one mouse, line represents the median.

(legend continued on next page)

LMP2A can develop, mature, and enter GCs, especially in gut-associated lymphoid organs.[33] In both cases, invader B cells were almost completely absent from the mLN GCs of the wild-type infected mouse at a time when substantial chimerism is observed when a wild-type naive partner is used (Figure 5J). As with naive partners, a large fraction of Tfh cells was parabiont-derived at this time point, indicative of successful chimerism (Figure 5J). We conclude that invasion of long-lived influenza-induced GCs is dependent on BCR sequence and is therefore not due to stochastic recruitment of bystander B cells.

Together, our data suggest a model in which late-stage clonal replacement is driven by entry into ongoing GCs of naive B cells that, although not detectably specific for influenza antigens, are still recruited in a BCR-dependent fashion. Invasion and eventual takeover of influenza-induced LLGCs by naive-derived B cell clones is therefore unlikely to involve affinity-dependent competition for binding to the same antigenic determinants recognized by GC founders[24] but more likely reflects a shift in the antigenic specificity of the entire GC.[23]

Long-term retention of influenza-specific GC B cells can lead to extensive affinity maturation

Despite progressive clonal replacement, minor but clear populations of fate-mapped B cells were still present in GCs as late as 24 wpi (Figure 2C). To gain insight into the nature of these cells, we searched the sequences of fate-mapped B cells at 24 wpi for expanded clones and built clonal phylogenies from their *Ighv* sequences (Figure 6A). We then selected 14 observed or inferred clonal burst points, from which we produced mAbs for affinity and specificity measurements. Three of the 14 clones assayed bound to lysates of influenza-infected MDCK cells by ELISA (Figure S5K). Two of these clones (F.07 and F.09) exclusively bound NP among our panel of recombinant influenza proteins (Figures 6B and S5L). On the other hand, clone F.01 bound to all influenza antigens assayed, although reactivity toward NP was detectable at 100-fold lower mAb concentrations than reactivity to the other proteins (Figure 6C, S5K, and S5L), suggesting that this clone is in fact NP specific. Clone F.01 also bound to all antigens of the classic polyreactivity panel (Figure 6D). Milder polyreactivity, directed primarily toward nucleic acids, was also observed for clone F.07. Both antibodies also bound lysates from uninfected MDCK cells (Figure S5K). Average Fab K_D values for the three-NP-binding mAbs ranged from 1.9×10^{-8} for clone F.01 to $<1.3 \times 10^{-10}$ M for clone F.09, which had an off rate longer than the limit of detection of our assay (Figure 6E). Taken together, these data indicate that long-term permanence in GCs can lead to a high degree of SHM and affinity maturation, potentially at the cost of acquiring polyreactivity.[34]

Founder-derived B cells in LLGCs contribute significantly to recall responses

The finding that founder clones can remain in LLGCs for extended periods prompted us to investigate the extent to which these clones contribute to recall responses. To this end, we fate-mapped GC B cells in PR8-infected S1pr2-Tomato mice at either 2 wpi (W2FM) or 12 wpi (W12FM), allowed fate-mapped GCs to export memory B cells until 16 wpi, then challenged these mice in the footpad with either recombinant NP or HA. We then measured plasmablast (PB) differentiation in the popliteal (p)LN 6 days later (Figures 7A and 7B). Fate-mapping resulted in the expected proportions of tdTomato$^+$ GC B cells in the mLN at the endpoint (Figure S6). Boosting generated similar amounts of pLN PBs in both fate-mapping regimens (Figures 7C and 7D). A substantial proportion (~20% or more) of PBs were fate-mapped in 3 of 4 and 1 of 4 NP- and HA-immunized pLN of W12FM mice, respectively. As expected, this proportion was somewhat lower than that obtained in W2FM mice (where mLN GCs exported memory B cells [MBCs] for an additional 10 weeks), but much higher than in control, age-matched uninfected (naive) mice given tamoxifen 4 weeks prior to boosting. To determine the origin of the fate-mapped PBs (Figure 7B), we sequenced the *Ig* genes of tdTomato$^-$ and tdTomato$^+$ PBs from the four W12FM pLNs with high PB fate-mapping. In general, recalled fate-mapped clones were substantially mutated (median of mean mutations per clone ranging from 7 to 16 *Ighv* nt in each boosted LN, higher than the value observed among non-fate-mapped clones; Figure 7E), suggestive of founder rather than invader origin. More importantly, 11 of 18 highly expanded tdTomato$^+$ clones (defined as clones representing >5% of that population) had clonal relatives in the tdTomato$^-$ population that were on average less mutated than their fate-mapped counterparts (Figures 7F–7H), suggesting that these clones were expanded prior to fate-mapping. Because the detection of both fate-mapped and non-fate-mapped progeny of the same clone is subject to statistical fluctuation, given the limited number of MBCs that generate the recall PB response,[14] 11 of 18 represents a lower bound in the proportion of tdTomato$^+$ clones with tdTomato$^-$ relatives. Therefore, most tdTomato$^+$ PBs are likely the progeny of founder clones exported as MBCs between 12 and 16 weeks post-immunization. Taken together, our findings indicate that founder clones in LLGCs continue to be an important source of recallable

(E) Mean *Ighv* SHM loads of tdTomato$^-$ and tdTomato$^+$ B cell clones sorted from pLN of NP or HA W12FM mice at 6 days post-boosting. Only pLN with substantial recruitment of fate-mapped B cells were analyzed. Data are from 4 mice from 2 independent experiments. Each symbol represents the mean SHM load of one clonal family. p values are for Student's t test.

(F) Pie charts showing clonal distribution of tdTomato$^+$ PBs as in (E). Highly expanded clones (representing >5% of sequenced cells in the compartment) are colored by whether or not sister cells bearing the same V(D)J rearrangement were identified in the non-fate-mapped PB compartment in the same node (not shown). Clones representing <5% of all cells are in dark gray. Numbers in the center of pies are number of clones/total cells sequenced. Roman numerals represent clones for which phylogenies are shown in (G).

(G) Clonal phylogenies for clones indicated in (F). Gray and red circles indicate sequences obtained from tdTomato$^-$ and tdTomato$^+$ cells, respectively. Identical sequences found in both compartments are represented as pie charts.

(H) Mean *Ighv* SHM load in tdTomato$^-$ and tdTomato$^+$ members of the same clone, obtained from clones with at least 5 cells from W12FM mice. p value is for paired Student's t test.

MBCs despite substantial clonal replacement, well into the 4th month of the influenza response.

DISCUSSION

Certain viral infections in mice are notorious for their ability to induce GC structures that persist for several months.[15–17,19] We show that rather than consisting of long-lived B cell clones, LLGCs primed by influenza and SARS-CoV-2 infection are maintained primarily by constant replacement of older clones by incoming naive B cells. In this sense, acutely induced but LLGCs resemble the truly chronic structures present in gut-associated lymphoid tissues and in autoimmune disease models, where turnover is expected, given the complex dynamics of the antigen source and the possibility of epitope spreading.[35,36] The finding that at least a fraction of invader clones accumulates somatic mutations and undergoes positive selection over time indicates that, as with gut-associated and autoimmune GCs, invader clones become active participants in the affinity maturation process, potentially shaping the evolution of founder clones themselves. On a global level, the outcome of clonal replacement is that average SHM levels in LLGCs fail to increase progressively and in fact decrease slightly over time in later months. Our finding that founder and invader clones appear to be competing within the same GCs, as evidenced both by clonal tree topologies and single-cell transcriptomic profiles, suggests that the founder response, rather than passively contracting, might be actively curtailed by clonal replacement. If this is the case, B cell invasion would be limiting the ability of LLGCs to produce B cells with high SHM loads.

Previous mechanistic studies where ongoing GCs are manipulated in various ways have set forth general rules for GC invasion. B cells specific for the antigen driving the ongoing GC have a short window of time to enter GCs during their formation. Late arrivers are allowed entry if they have higher affinity than the cells currently in the GC or if they are previously pulsed with antigen *ex vivo* in immunization models.[24,37] High-affinity monoclonal B cells are allowed entry into GCs in lymphocytic choriomeningitis virus (LCMV)-infected mice when transferred at 20 days post infection, with greater participation in mice infected with the more persistent LCMV clone 13 than with the short-lived Armstrong strain, suggesting higher local concentrations of antigen may favor such early invasion.[38] On the other hand, sequential immunization with different antigens allows abundant invasion of ongoing GCs independently of the invader's affinity,[23] presumably because in this setting founder and invader B cells do not compete for the same Tfh cells. We show that GC invasion is highly polyclonal and therefore unlikely to derive from massive expansion of rare naive clones with higher affinity than the previously matured B cells already present in the GC. More importantly, the B cells that invade influenza-induced LLGCs failed to bind to recombinant influenza antigens, even when antibodies are produced from strongly positively selected invader clones and antigens are multimerized, arguing for a mechanism distinct from that observed in LCMV infection.[38] One possible explanation is that late invaders bind cryptic forms of viral antigens not captured by recombinant protein-based assays,[28] potentially because ingress of B cell clones binding well-formed antigens is inhibited by antibody mediated feedback.[39] Another interpretation is that late-GC invaders, rather than having higher affinity than founders, are driven by a separate GC reaction of different specificity taking place within the same GC structure. Our finding that Tfh cells also turn over substantially at later time points (Figure S3) provides additional support to the latter model.

mAbs cloned from positively selected invader B cells did not consistently bind common self-antigens and uninfected cell lysates. Therefore, invaders do not appear to be specific for self-antigens, as shown, for example, in GC B cells elicited by zika virus infection.[40] Because the respiratory mucosa is exposed to microbial antigens both from the environment (which, in normal mouse housing conditions is rich in mouse fecal bacteria) and derived from respiratory tract-resident commensals,[41,42] one possibility is that invader clones could be specific for microbial products. Screening of invader-derived antibodies against gut microbiota[36] produced negative results; however, one cannot rule out specificity toward microbial antigens exclusively present on respiratory-tract commensals or other environmental antigens (e.g., from food or bedding) to which the lung mucosa is exposed and that may drain into the mLN. If this is the case, a potential explanation for the larger size of post-infection GCs compared with the spontaneous reactions found in unimmunized mice of the same age[19] is that an ongoing GC reaction to viral antigens could facilitate access of environmental antigen-specific B cells to previously formed GC structures, performing an adjuvant-like function for non-influenza-specific GC B cells.

Despite extensive replacement, a small number of founder B cell clones persisted in GCs for up to 24 weeks, accumulating dozens of somatic mutations over several months. Some of these cells were found to bind strongly to influenza antigens, with K_Ds in the order of 10 nM to <100 pM and extremely long off rates. Importantly, these clones are capable of exporting MBCs that are usable in recall responses to isolated viral antigens. This finding is in agreement with a previous report that used nucleotide pulsing to show that influenza-induced GCs export HA-binding MBCs between 7 and 12.5 wpi, although these kinetics only partly overlap with our definition of a late GC (>12 wpi).[19] Therefore, despite pronounced clonal turnover, LLGCs still have the potential to generate recallable MBCs with extreme degrees of SHM and affinity maturation. Further understanding of the extent to which clonal turnover impairs or potentially even contributes to these long evolutionary trajectories may improve our ability to generate such exceptional clones at higher frequencies.

Limitations of the study

We were unable to determine the antigenic specificity of invader B cell clones and therefore cannot rule out that invader B cell clones may be specific for cryptic forms of influenza antigens (e.g., misfolded proteins or proteolytic degradation products) not represented in our ELISA or BLI assays using recombinant proteins. Such "dark antigen" has been proposed as a potential

trigger for the non-antigen binding clones that are frequently detected in acute immunization-induced GCs[28] and represents a general caveat of studies of polyclonal immune responses.[43] Moreover, the unavailability of experimental approaches to prevent GC invasion prevented us from directly testing the hypothesis that clonal replacement inhibits accumulation of founders with high SHM. Future development of genetic or other strategies to prevent invasion will be required to address this question.

STAR★METHODS

Detailed methods are provided in the online version of this paper and include the following:

- KEY RESOURCES TABLE
- RESOURCE AVAILABILITY
  - Lead contact
  - Materials availability
  - Data and code availability
- EXPERIMENTAL MODEL AND SUBJECT DETAILS
  - Experimental mice
  - Cell lines
- METHOD DETAILS
  - Infection models and fate-mapping
  - Parabiosis
  - Multiphoton imaging of mLNs
  - Flow cytometry and cell sorting
  - Single-GC B cell cultures
  - *Ig* sequencing at single-cell level
  - Analysis of sequencing data
  - scRNA-seq library preparation and analysis
  - Monoclonal antibody production and binding measurements
  - Preparation of fecal bacteria for ELISA
  - ELISA
- QUANTIFICATION AND STATISTICAL ANALYSIS

SUPPLEMENTAL INFORMATION

Supplemental information can be found online at https://doi.org/10.1016/j.cell.2022.11.031.

ACKNOWLEDGMENTS

We thank all members of the Victora Laboratory for helpful discussion, Rockefeller University staff for support, K. Gordon for FACS sorting, M. Kaneiko and A. McDermott (NIH/NIAID/VRC) for HA tetramers, T. Randall (University of Alabama, Birmingham I) for NP tetramers, F. Krammer (Mt. Sinai School of Medicine) for recombinant influenza antigens, G. Kelsoe (Duke University) for NB-21.2D9 cells, T. Kurosaki and T. Okada (Osaka University and RIKEN-Yokohama) for S1pr2-CreERT2 mice, and K. Rajewsky (Max Delbrück Center for Molecular Medicine) and M. Iannacone (San Raffaele Research Institute) for DH-LMP2A mice. This work was funded by NIH/NIAID grants R01AI119006, R01AI139117, and R01AI157137 to G.D.V. Work in the Victora lab is additionally supported by NIH grant DP1AI144248 (Pioneer award) and the Robertson Foundation. P.J.U. was supported by NIH/NIAID grants R01AI125197-04 and U01AI150741-01S1 and by the Henry Gustav Floren Trust. J.E. was supported by a CRI Irvington postdoctoral fellowship. R.V.d.H.C. is supported by HFSP fellowship LT000892/2020-L. A.B. is supported by NIAID grant F30AI157448, Louis and Rachel Rudin Fellowship in Immunology, and NIGMS Medical Scientist Training Program grant T32GM007739. J.T.J. was supported by the Research Council of Norway and COFUND – Marie Curie Actions program. M.C.C.C. is a Pew Latin-American Fellow. G.D.V. is a Burroughs Wellcome Investigator in the Pathogenesis of Infectious Disease, a Pew-Stewart Scholar, and a MacArthur Fellow. We dedicate this article to the memory of J.E.

AUTHOR CONTRIBUTIONS

R.V.H.d.C., J.E., and A.B. performed most experimental work with assistance from L.M., A.H., J.T.J., M.C.C.C., R.P., and C.R.N. T.B.R.C. analyzed and interpreted scRNA-seq data. H.-H.H. assisted with SARS-CoV-2 infection. R.V.H.d.C., J.E., A.B., and G.D.V. conceptualized the work, designed all experiments, and analyzed the data. R.V.H.d.C., A.B., and G.D.V. wrote the manuscript. With the exception of J.E. (deceased), all authors reviewed, edited, and approved the final version of the manuscript.

DECLARATION OF INTERESTS

G.D.V. is an advisor for Vaccine Company, Inc.

INCLUSION AND DIVERSITY

The authors support inclusive, diverse, and equitable conduct of research.

Received: April 13, 2022
Revised: September 12, 2022
Accepted: November 28, 2022
Published: December 23, 2022

REFERENCES

1. Mesin, L., Ersching, J., and Victora, G.D. (2016). Germinal center B cell dynamics. Immunity *45*, 471–482. https://doi.org/10.1016/j.immuni.2016.09.001.
2. Victora, G.D., and Nussenzweig, M.C. (2022). Germinal centers. Annu. Rev. Immunol. *40*, 413–442. https://doi.org/10.1146/annurev-immunol-120419-022408.
3. Cyster, J.G., and Allen, C.D.C. (2019). B cell responses: cell interaction dynamics and decisions. Cell *177*, 524–540. https://doi.org/10.1016/j.cell.2019.03.016.
4. Elsner, R.A., and Shlomchik, M.J. (2020). Germinal center and extrafollicular B cell responses in vaccination, immunity, and autoimmunity. Immunity *53*, 1136–1150. https://doi.org/10.1016/j.immuni.2020.11.006.
5. Kepler, T.B., and Perelson, A.S. (1993). Cyclic re-entry of germinal center B cells and the efficiency of affinity maturation. Immunol. Today *14*, 412–415.
6. Victora, G.D., Schwickert, T.A., Fooksman, D.R., Kamphorst, A.O., Meyer-Hermann, M., Dustin, M.L., and Nussenzweig, M.C. (2010). Germinal center dynamics revealed by multiphoton microscopy with a photoactivatable fluorescent reporter. Cell *143*, 592–605. https://doi.org/10.1016/j.cell.2010.10.032.
7. Victora, G.D., and Mouquet, H. (2018). What are the primary limitations in B-cell affinity maturation, and how much affinity maturation can we drive with vaccination? Lessons from the antibody response to HIV-1. Cold Spring Harb. Perspect. Biol. *10*, a029397. https://doi.org/10.1101/cshperspect.a029389.
8. Scheid, J.F., Mouquet, H., Ueberheide, B., Diskin, R., Klein, F., Oliveira, T.Y., Pietzsch, J., Fenyo, D., Abadir, A., Velinzon, K., et al. (2011). Sequence and structural convergence of broad and potent HIV antibodies that mimic CD4 binding. Science *333*, 1633–1637. https://doi.org/10.1126/science.1207227.
9. Klein, F., Diskin, R., Scheid, J.F., Gaebler, C., Mouquet, H., Georgiev, I.S., Pancera, M., Zhou, T., Incesu, R.B., Fu, B.Z., et al. (2013). Somatic mutations of the immunoglobulin framework are generally required for broad

and potent HIV-1 neutralization. Cell *153*, 126–138. https://doi.org/10.1016/j.cell.2013.03.018.

10. Wiehe, K., Bradley, T., Meyerhoff, R.R., Hart, C., Williams, W.B., Easterhoff, D., Faison, W.J., Kepler, T.B., Saunders, K.O., Alam, S.M., et al. (2018). Functional relevance of improbable antibody mutations for HIV broadly neutralizing antibody development. Cell Host Microbe *23*. 759.e6–765.e6. https://doi.org/10.1016/j.chom.2018.04.018.

11. Burton, D.R., Ahmed, R., Barouch, D.H., Butera, S.T., Crotty, S., Godzik, A., Kaufmann, D.E., McElrath, M.J., Nussenzweig, M.C., Pulendran, B., et al. (2012). A blueprint for HIV vaccine discovery. Cell Host Microbe *12*, 396–407. https://doi.org/10.1016/j.chom.2012.09.008.

12. Liu, Y.J., Zhang, J., Lane, P.J., Chan, E.Y., and MacLennan, I.C. (1991). Sites of specific B cell activation in primary and secondary responses to T cell-dependent and T cell-independent antigens. Eur. J. Immunol. *21*, 2951–2962. https://doi.org/10.1002/eji.1830211209.

13. Kasturi, S.P., Skountzou, I., Albrecht, R.A., Koutsonanos, D., Hua, T., Nakaya, H.I., Ravindran, R., Stewart, S., Alam, M., Kwissa, M., et al. (2011). Programming the magnitude and persistence of antibody responses with innate immunity. Nature *470*, 543–547. https://doi.org/10.1038/nature09737.

14. Mesin, L., Schiepers, A., Ersching, J., Barbulescu, A., Cavazzoni, C.B., Angelini, A., Okada, T., Kurosaki, T., and Victora, G.D. (2020). Restricted clonality and limited germinal center reentry characterize memory B cell reactivation by boosting. Cell *180*. 92–106.e11. https://doi.org/10.1016/j.cell.2019.11.032.

15. Bachmann, M.F., Odermatt, B., Hengartner, H., and Zinkernagel, R.M. (1996). Induction of long-lived germinal centers associated with persisting antigen after viral infection. J. Exp. Med. *183*, 2259–2269. https://doi.org/10.1084/jem.183.5.2259.

16. Rothaeusler, K., and Baumgarth, N. (2010). B-cell fate decisions following influenza virus infection. Eur. J. Immunol. *40*, 366–377. https://doi.org/10.1002/eji.200939798.

17. Adachi, Y., Onodera, T., Yamada, Y., Daio, R., Tsuiji, M., Inoue, T., Kobayashi, K., Kurosaki, T., Ato, M., and Takahashi, Y. (2015). Distinct germinal center selection at local sites shapes memory B cell response to viral escape. J. Exp. Med. *212*, 1709–1723. https://doi.org/10.1084/jem.20142284.

18. Gaebler, C., Wang, Z., Lorenzi, J.C.C., Muecksch, F., Finkin, S., Tokuyama, M., Cho, A., Jankovic, M., Schaefer-Babajew, D., Oliveira, T.Y., et al. (2021). Evolution of antibody immunity to SARS-CoV-2. Nature *591*, 639–644. https://doi.org/10.1038/s41586-021-03207-w.

19. Yewdell, W.T., Smolkin, R.M., Belcheva, K.T., Mendoza, A., Michaels, A.J., Cols, M., Angeletti, D., Yewdell, J.W., and Chaudhuri, J. (2021). Temporal dynamics of persistent germinal centers and memory B cell differentiation following respiratory virus infection. Cell Rep. *37*, 109961. https://doi.org/10.1016/j.celrep.2021.109961.

20. Shinnakasu, R., Inoue, T., Kometani, K., Moriyama, S., Adachi, Y., Nakayama, M., Takahashi, Y., Fukuyama, H., Okada, T., and Kurosaki, T. (2016). Regulated selection of germinal-center cells into the memory B cell compartment. Nat. Immunol. *17*, 861–869. https://doi.org/10.1038/ni.3460.

21. Shulman, Z., Gitlin, A.D., Targ, S., Jankovic, M., Pasqual, G., Nussenzweig, M.C., and Victora, G.D. (2013). T follicular helper cell dynamics in germinal centers. Science *341*, 673–677. https://doi.org/10.1126/science.1241680.

22. Dinnon, K.H., 3rd, Leist, S.R., Schäfer, A., Edwards, C.E., Martinez, D.R., Montgomery, S.A., West, A., Yount, B.L., Jr., Hou, Y.J., Adams, L.E., et al. (2020). A mouse-adapted model of SARS-CoV-2 to test COVID-19 countermeasures. Nature *586*, 560–566. https://doi.org/10.1038/s41586-020-2708-8.

23. Schwickert, T.A., Alabyev, B., Manser, T., and Nussenzweig, M.C. (2009). Germinal center reutilization by newly activated B cells. J. Exp. Med. *206*, 2907–2914. https://doi.org/10.1084/jem.20091225.

24. Schwickert, T.A., Lindquist, R.L., Shakhar, G., Livshits, G., Skokos, D., Kosco-Vilbois, M.H., Dustin, M.L., and Nussenzweig, M.C. (2007). In vivo imaging of germinal centres reveals a dynamic open structure. Nature *446*, 83–87.

25. Tas, J.M., Mesin, L., Pasqual, G., Targ, S., Jacobsen, J.T., Mano, Y.M., Chen, C.S., Weill, J.C., Reynaud, C.A., Browne, E.P., et al. (2016). Visualizing antibody affinity maturation in germinal centers. Science *351*, 1048–1054. https://doi.org/10.1126/science.aad3439.

26. Pae, J., Ersching, J., Castro, T.B.R., Schips, M., Mesin, L., Allon, S.J., Ordovas-Montanes, J., Mlynarczyk, C., Melnick, A., Efeyan, A., et al. (2021). Cyclin D3 drives inertial cell cycling in dark zone germinal center B cells. J. Exp. Med. *218*, e20201699. https://doi.org/10.1084/jem.20201699.

27. Ramezani-Rad, P., Chen, C., Zhu, Z., and Rickert, R.C. (2020). Cyclin D3 governs clonal expansion of dark zone germinal center B cells. Cell Rep. *33*, 108403. https://doi.org/10.1016/j.celrep.2020.108403.

28. Kuraoka, M., Schmidt, A.G., Nojima, T., Feng, F., Watanabe, A., Kitamura, D., Harrison, S.C., Kepler, T.B., and Kelsoe, G. (2016). Complex antigens drive permissive clonal selection in germinal centers. Immunity *44*, 542–552. https://doi.org/10.1016/j.immuni.2016.02.010.

29. Krammer, F., Smith, G.J.D., Fouchier, R.A.M., Peiris, M., Kedzierska, K., Doherty, P.C., Palese, P., Shaw, M.L., Treanor, J., Webster, R.G., and García-Sastre, A. (2018). Influenza. Nat. Rev. Dis. Primers *4*, 3. https://doi.org/10.1038/s41572-018-0002-y.

30. Viant, C., Weymar, G.H.J., Escolano, A., Chen, S., Hartweger, H., Cipolla, M., Gazumyan, A., and Nussenzweig, M.C. (2020). Antibody affinity shapes the choice between memory and germinal center B cell fates. Cell *183*. 1298–1311.e11. https://doi.org/10.1016/j.cell.2020.09.063.

31. Lee, J., Boutz, D.R., Chromikova, V., Joyce, M.G., Vollmers, C., Leung, K., Horton, A.P., DeKosky, B.J., Lee, C.H., Lavinder, J.J., et al. (2016). Molecular-level analysis of the serum antibody repertoire in young adults before and after seasonal influenza vaccination. Nat. Med. *22*, 1456–1464. https://doi.org/10.1038/nm.4224.

32. Goodnow, C.C., Crosbie, J., Adelstein, S., Lavoie, T.B., Smith-Gill, S.J., Brink, R.A., Pritchard-Briscoe, H., Wotherspoon, J.S., Loblay, R.H., and Raphael, K. (1988). Altered immunoglobulin expression and functional silencing of self-reactive B lymphocytes in transgenic mice. Nature *334*, 676–682.

33. Casola, S., Otipoby, K.L., Alimzhanov, M., Humme, S., Uyttersprot, N., Kutok, J.L., Carroll, M.C., and Rajewsky, K. (2004). B cell receptor signal strength determines B cell fate. Nat. Immunol. *5*, 317–327. https://doi.org/10.1038/ni1036.

34. Mouquet, H., Scheid, J.F., Zoller, M.J., Krogsgaard, M., Ott, R.G., Shukair, S., Artyomov, M.N., Pietzsch, J., Connors, M., Pereyra, F., et al. (2010). Polyreactivity increases the apparent affinity of anti-HIV antibodies by heteroligation. Nature *467*, 591–595. https://doi.org/10.1038/nature09385.

35. Degn, S.E., van der Poel, C.E., Firl, D.J., Ayoglu, B., Al Qureshah, F.A., Bajic, G., Mesin, L., Reynaud, C.A., Weill, J.C., Utz, P.J., et al. (2017). Clonal evolution of autoreactive germinal centers. Cell *170*. 913–926.e19. https://doi.org/10.1016/j.cell.2017.07.026.

36. Nowosad, C.R., Mesin, L., Castro, T.B.R., Wichmann, C., Donaldson, G.P., Araki, T., Schiepers, A., Lockhart, A.A.K., Bilate, A.M., Mucida, D., and Victora, G.D. (2020). Tunable dynamics of B cell selection in gut germinal centres. Nature *588*, 321–326. https://doi.org/10.1038/s41586-020-2865-9.

37. Turner, J.S., Benet, Z.L., and Grigorova, I.L. (2017). Antigen acquisition enables newly arriving B cells to enter ongoing immunization-induced germinal centers. J. Immunol. *199*, 1301–1307. https://doi.org/10.4049/jimmunol.1700267.

38. Fallet, B., Hao, Y., Florova, M., Cornille, K., de Los Aires, A.V., Girelli Zubani, G., Ertuna, Y.I., Greiff, V., Menzel, U., Hammad, K., et al. (2020). Chronic viral infection promotes efficient germinal center B cell responses. Cell Rep. *30*. 1013–1026.e7. https://doi.org/10.1016/j.celrep.2019.12.023.

39. Tas, J.M.J., Koo, J.-H., Lin, Y.-C., Xie, Z., Steichen, J.M., Jackson, A.M., Hauser, B.M., Wang, X., Cottrell, C.A., Torres, J.L., et al. (2022). Antibodies from primary humoral responses modulate the recruitment of naive B cells during secondary responses. Immunity *55*. 1856–1871.e6. https://doi.org/10.1016/j.immuni.2022.07.020.

40. Cavazzoni, C.B., Bozza, V.B.T., Lucas, T.C.V., Conde, L., Maia, B., Mesin, L., Schiepers, A., Ersching, J., Neris, R.L.S., Conde, J.N., et al. (2021). The immunodominant antibody response to Zika virus NS1 protein is characterized by cross-reactivity to self. J. Exp. Med. *218*, e20210580. https://doi.org/10.1084/jem.20210580.

41. Dickson, R.P., Erb-Downward, J.R., Martinez, F.J., and Huffnagle, G.B. (2016). The microbiome and the respiratory tract. Annu. Rev. Physiol. *78*, 481–504. https://doi.org/10.1146/annurev-physiol-021115-105238.

42. Jin, C., Lagoudas, G.K., Zhao, C., Bullman, S., Bhutkar, A., Hu, B., Ameh, S., Sandel, D., Liang, X.S., Mazzilli, S., et al. (2019). Commensal microbiota promote lung cancer development via γδ T cells. Cell *176*. 998–1013.e16. https://doi.org/10.1016/j.cell.2018.12.040.

43. Abbott, R.K., and Crotty, S. (2020). Factors in B cell competition and immunodominance. Immunol. Rev. *296*, 120–131. https://doi.org/10.1111/imr.12861.

44. Madisen, L., Zwingman, T.A., Sunkin, S.M., Oh, S.W., Zariwala, H.A., Gu, H., Ng, L.L., Palmiter, R.D., Hawrylycz, M.J., Jones, A.R., et al. (2010). A robust and high-throughput Cre reporting and characterization system for the whole mouse brain. Nat. Neurosci. *13*, 133–140. https://doi.org/10.1038/nn.2467.

45. Crouch, E.E., Li, Z., Takizawa, M., Fichtner-Feigl, S., Gourzi, P., Montaño, C., Feigenbaum, L., Wilson, P., Janz, S., Papavasiliou, F.N., and Casellas, R. (2007). Regulation of AID expression in the immune response. J. Exp. Med. *204*, 1145–1156. https://doi.org/10.1084/jem.20061952.

46. Coleman, D.L., and Hummel, K.P. (1969). Effects of parabiosis of normal with genetically diabetic mice. Am. J. Physiol. *217*, 1298–1304. https://doi.org/10.1152/ajplegacy.1969.217.5.1298.

47. Harris, R.B. (1997). Loss of body fat in lean parabiotic partners of ob/ob mice. Am. J. Physiol. *272*, R1809–R1815. https://doi.org/10.1152/ajpregu.1997.272.6.R1809.

48. Trombetta, J.J., Gennert, D., Lu, D., Satija, R., Shalek, A.K., and Regev, A. (2014). Preparation of single-cell RNA-seq libraries for next generation sequencing. Curr. Protoc. Mol. Biol. *107*, 4.22.1–4.22.17. https://doi.org/10.1002/0471142727.mb0422s107.

49. Han, A., Glanville, J., Hansmann, L., and Davis, M.M. (2014). Linking T-cell receptor sequence to functional phenotype at the single-cell level. Nat. Biotechnol. *32*, 684–692.

50. Masella, A.P., Bartram, A.K., Truszkowski, J.M., Brown, D.G., and Neufeld, J.D. (2012). PANDAseq: paired-end assembler for Illumina sequences. BMC Bioinformatics *13*, 31. https://doi.org/10.1186/1471-2105-13-31.

51. Lefranc, M.P., Giudicelli, V., Ginestoux, C., Jabado-Michaloud, J., Folch, G., Bellahcene, F., Wu, Y., Gemrot, E., Brochet, X., Lane, J., et al. (2009). IMGT, the international ImMunoGeneTics information system. Nucleic Acids Res. *37*, D1006–D1012. https://doi.org/10.1093/nar/gkn838.

52. Retter, I., Althaus, H.H., Münch, R., and Müller, W. (2005). VBASE2, an integrative V gene database. Nucleic Acids Res. *33*, D671–D674. https://doi.org/10.1093/nar/gki088.

53. DeWitt, W.S., 3rd, Mesin, L., Victora, G.D., Minin, V.N., and Matsen, F.A.t. (2018). Using genotype abundance to improve phylogenetic inference. Mol. Biol. Evol. *35*, 1253–1265. https://doi.org/10.1093/molbev/msy020.

54. Hafemeister, C., and Satija, R. (2019). Normalization and variance stabilization of single-cell RNA-seq data using regularized negative binomial regression. Genome Biol. *20*, 296. https://doi.org/10.1186/s13059-019-1874-1.

55. Stuart, T., Butler, A., Hoffman, P., Hafemeister, C., Papalexi, E., Mauck, W.M., 3rd, Hao, Y., Stoeckius, M., Smibert, P., and Satija, R. (2019). Comprehensive integration of single-cell data. Cell *177*. 1888–1902.e21. https://doi.org/10.1016/j.cell.2019.05.031.

56. Tirosh, I., Izar, B., Prakadan, S.M., Wadsworth, M.H., 2nd, Treacy, D., Trombetta, J.J., Rotem, A., Rodman, C., Lian, C., Murphy, G., et al. (2016). Dissecting the multicellular ecosystem of metastatic melanoma by single-cell RNA-seq. Science *352*, 189–196. https://doi.org/10.1126/science.aad0501.

57. Schuhmacher, M., Kohlhuber, F., Hölzel, M., Kaiser, C., Burtscher, H., Jarsch, M., Bornkamm, G.W., Laux, G., Polack, A., Weidle, U.H., and Eick, D. (2001). The transcriptional program of a human B cell line in response to Myc. Nucleic Acids Res. *29*, 397–406.

STAR★METHODS

KEY RESOURCES TABLE

REAGENT or RESOURCE	SOURCE	IDENTIFIER
Antibodies		
Anti-Mo TCR beta, eBioscience™	Invitrogen	47-5961-82
BV 650 anti-mouse CD138 (Syndecan-1)	BioLegend	142517
BV 785 anti-mouse/human CD45R/B220	BioLegend	103246
PE-Cy7 Hamster Anti-Mouse CD95	BD Biosciences	557653
Anti-Mouse CD38 APC	Invitrogen	17-0381-82
AlexaFluor ® 700 anti-mouse/human CD45.1	BioLegend	110724
APC/Cy7 anti-mouse CD45.1	BioLegend	110715
BV421 anti-mouse CD45.1	BioLegend	110731
BV 605 anti-mouse CD45.2	BioLegend	109841
BV 785 ™ anti-mouse CD45.2	BioLegend	109839
PE/Cy7 anti-mouse CD45.2	BioLegend	109830
APC anti-mouse CD279 (PD-1)	BioLegend	135210
PE/Cy7 anti-mouse CD279 (PD-1)	BioLegend	109110
BV 650 anti-mouse CD185 (CXCR5)	BioLegend	145517
Bacterial and virus strains		
Influenza PR8	Michael Carroll, Harvard Medical School	N/A
SARS-CoV-2 MA10	Dinnon et al. [22]	N/A
Chemicals, peptides, and recombinant proteins		
Alhydrogel 2%	InvivoGen	vac-alu-250
HA-biotinylated tetramer	Victora Lab	N/A
Nucleoprotein (NP)	SinoBiological	11675-V08B
Spike-biotinylated tetramer	Sino Biological	40592-V27B-B
BB515 Streptavidin	BD Biosciences	564453
PerCP Streptavidin	BioLegend	405213
Anti-Human Fab-CH1 2nd Generation (FAB2G)	ForteBio	18-5125
EZ-Link™ Sulfo NHS-LC-LC-Biotin, No-Weigh™ Format	Thermo Scientific	A35358
TCL Buffer	QIAGEN	1031576
2-Mercaptoethanol	Thermo Fisher Scientific	21985023
Tamoxifen	Sigma-Aldrich	T5648-5G
Corn oil	Sigma-Aldrich	C8267-500ML
Bovine Serum Albumin (BSA)	Sigma-Aldrich	A9647-500G
FreeStyle 293 Expression Medium	Thermo Fisher Scientific	12338026
OptiPRO SFM Medium	Thermo Fisher Scientific	12309019
Meloxicam	Patterson Veterinary	26637-621-0
Critical commercial assays		
High Precision Streptavidin (SAX) Dip and Read™ Biosensors	ForteBio	18-5118
Agencourt RNAClean XP kit	Beckman Coulter	A63987
Zeba desalting column purification	Thermo Fisher Scientific	89883
RT maxima reverse transcriptase	Thermo Fisher Scientific	EP0753
MiSeq Reagent Nano Kit v2 (500-cycles)	Illumina	MS-103-1003
Protein G Sepharose 4 Fast Flow	GE Healthcare	17-0618-01
Ni Sepharose Excel	GE Healthcare	17371201

(*Continued on next page*)

Continued		
REAGENT or RESOURCE	SOURCE	IDENTIFIER
Deposited data		
scRNAseq data	This paper	GEO: GSE218165
Experimental models: Cell lines		
Human Freestyle 293F cell	ThermoFisher	R79007
NB-21.2D9 cell	Kuraoka et al. [28]	N/A
Experimental models: Organisms/strains		
C57BL/6J mice	JacksonLabs	000664
B6.SJL-Ptprc^{a} Pepc^{b}/BoyJ	JacksonLabs	002014
B6.Cg-Gt(ROSA)26Sor$^{tm14(CAG-tdTomato)Hze}$/J	Madisen et al.[44]	N/A
C57BL/6-Tg(Aicda/EGFP)1Rcas/J	Crouch et al.[45]	N/A
C57BL/6-(Tg(IghelMD4)4Ccg/J	Goodnow et al.[32]	N/A
Tg(UBC-PA-GFP)1Mnz/J	Victora et al.[6]	N/A
S1pr2^{CreERT2}	Shinnakasu et al. [20]	N/A
Igh^{LMP2A}	Casola et al. [33]	N/A
Software and algorithms		
FlowJo Tree Star software	FlowJo LLC	https://www.flowjo.com/solutions/flowjo/downloads
GraphPad Prism 8.0	GraphPad Software	https://www.graphpad.com/scientific-software/prism/
Adobe Illustrator	Adobe Illustrator (Ai)	https://www.adobe.com/products/illustrator.html

RESOURCE AVAILABILITY

Lead contact

Further information and request for resources and any reagents should be directly fulfilled by Gabriel D. Victora (victora@rockefeller.edu), lead contact of this study.

Materials availability

Antibodies, reagents, and mouse strains used in this study can be requested from the lead contact.

Data and code availability

scRNA-seq datasets are available from Gene Expression Omnibus (GEO), under ID GSE218165. Any additional information required to reanalyze the data reported in this paper is available from the lead contact upon request.

EXPERIMENTAL MODEL AND SUBJECT DETAILS

Experimental mice

All mice used in this study were held under specific pathogen-free conditions at the Rockefeller University Comparative for Biosciences Center. All experimental procedures were approved by the Rockefeller University's Institutional Animal Care and Use Committee. Wild-type C57BL/6J, B6 CD45.1 (B6.SJL-*Ptprc*^{a} *Pepc*^{b}/BoyJ), *Rosa26*$^{Stop\text{-}tdTomato}$ (B6.Cg-*Gt(ROSA)26Sor*$^{tm14(CAG\text{-}tdTomato)Hze}$/J),[44] AID-GFP transgenic (C57BL/6-Tg(Aicda/EGFP)1Rcas/J)[45]; and MD-4 BCR transgenic C57BL/6-(Tg(IghelMD4)4Ccg/J)[32] mice were obtained from The Jackson Laboratory. PA-GFP transgenic mice (Tg(UBC-PA-GFP)1Mnz/J)[6] were generated and maintained at the Rockefeller University. *S1pr2*^{CreERT2} BAC-transgenic mice[20] were generated and kindly provided by T. Kurosaki and T. Okada (Osaka University and RIKEN-Yokohama). D_H-LMP2A (*Igh*^{LMP2A}) mice[33] were generated by K. Rajewsky (Max Delbrück Center for Molecular Medicine, Germany) and backcrossed into the C57BL/6 background and kindly provided by M. Iannacone (San Raffaele Research Institute, Italy). Mice used in this study were female and male adults ranging from 8 to 12 weeks-old.

Cell lines

The human Freestyle 293F cell line was used to produce recombinant antibodies and Fabs. Human Freestyle 293F cells were grown in FreeStyle 293 Expression Medium at 37°C, 8% CO2 and 135RPM. The NB-21.2D9 cell line used for single GC B cell cultures was kindly provided by Garnett Kelsoe.[28] NB-21.2D9 cells were grown in OptiMEM (Invitrogen) supplemented with 10% HyClone FBS (Thermo), 10 mM HEPES, 2mM L-glutamine, 1 mM sodium pyruvate, 50 μM 2-mercaptoethanol, 100 μg/ml penicillin, 100 μg/ml streptomycin, 1 mM vitamins, and 1 mM non-essential amino acids (all from Invitrogen) at 37°C and 5% CO2.

METHOD DETAILS

Infection models and fate-mapping

Animals were anesthetized with ketamine/xylazine diluted in sterile PBS 1X (Gibco, Inc.) and infected intranasally with 33 PFU of mouse-adapted influenza PR8 virus (provided by M. Carroll, Harvard Medical School). For SARS-CoV-2 infection, anesthetized mice were given $3x10^3$ PFU of mouse-adapted SARS-CoV-2 intranasally, as previously described.[22] Fate-mapping of GCs in S1pr2-Tomato mice was carried out by intragastric administration of a single 2.5 mg dose of tamoxifen citrate (Sigma Aldrich) diluted in corn oil. Immunizations were carried out in the hind footpads using 5 μg of recombinant HA and NP diluted in 1/3 volume of alhydrogel (InvivoGen). All experiments were performed according to institutional guidelines and were approved by the Rockefeller University institutional animal care and use committee (Protocol number 19033-H).

Parabiosis

Infected mice were fate-mapped (whenever S1pr2-Tomato was used) at week 2 after infection, and joined parabiotically to a naïve or infected mouse at 4 weeks after infection. Parabiosis surgeries were performed as previously described.[46,47] Briefly, anesthesia was induced with isoflurane (1.5%–2%), after which incisions spanning 2 inches were made longitudinally along one flank of each mouse, from the elbow to the knee. Mice were sutured together by the femurs and humeri, and sutures and wound clips were used to join the skin. For analgesia, both Buprenorphine (0.1 mg/kg) and Meloxicam (2 mg/kg) were administered subcutaneously immediately prior to surgery and 24 and 48 h after surgery. At different time points after the surgery, pairs were sacrificed and the draining mediastinal LN was harvested for various readouts. Mice displaying less than 30% naïve B cell chimerism at the time point of interest were excluded from the analysis.

Multiphoton imaging of mLNs

Mediastinal LNs (mLNs) were harvested at least 8 weeks after initial infection and detached from adipose tissue with the aid of a dissecting microscope. Nodes were then placed in PBS between two coverslips sealed together with vacuum grease. The tissue was kept on a cooled metal block throughout the preparation and during the imaging. Multiphoton imaging was performed as described,[25] using an Olympus FV1000 upright microscope fitted with a 25X 1.05NA Plan water-immersion objective and a Mai-Tai DeepSee Ti-Sapphire laser (Spectraphysics). For labeling FDC networks *in vivo*, 10 μg of an anti-CD35 antibody (clone 8C12) conjugated to Alexa-633 was administered intravenously 24-48 hours before imaging. LN tissues isolated from S1pr2-Tomato mice were imaged at l = 930 nm for tdTomato. To sort cells from single GCs, we performed photoactivation on PAGFP-transgenic mice crossed to *S1pr2*$^{CreERT2/+}$*Rosa26*$^{Stop\text{-}tdTomato}$, as previously described. Briefly, clusters of tdTomato$^+$ cells were identified by imaging at λ = 1000 nm, at which no photoactivation is observed, and 3D regions of interest were photoactivated by higher-power scanning at λ = 830 nm.

Flow cytometry and cell sorting

For flow cytometry and cell sorting, disposable micropestles (Axygen) were used to mechanically disassociate LNs into cell suspensions. Cells from each tissue were resuspended in PBE 1X (PBS supplemented with 0.5% BSA + 1 mM EDTA) and incubated for 30 min on ice with fluorescently-labeled antibodies described in the key resources table. Cells were filtered and washed with PBE again before analysis on BD FACS LSR II or FACS Symphony cytometers and sorting on FACS ARIA II cytometers. Analyses were performed using FlowJo v. 10 software.

Single-GC B cell cultures

NB-21.2D9 feeder cells expressing CD40L, BAFF, and IL-21[28] (kindly provided by Garnett Kelsoe, Duke University) were seeded the day before B cell sorting into 96-well round-bottom plates (Corning) at 2,500 cells/well. On the day of single GC B cell sorting, cultures were supplemented with 4 ng/ml of recombinant IL-4 (R&D Systems) and *Salmonella typhimurium* LPS (Sigma-Aldrich). Supernatants were harvested on day 7 of culture.

Ig sequencing at single-cell level

Single GC B cells were index-sorted into 96-well plates containing 5 ml TCL buffer (QIAGEN) supplemented with 1% β-mercaptoethanol. SPRI beads were used to extract nucleic acids as previously described.[25,48] RT maxima reverse transcriptase (Thermo Scientific) with oligo(dT) as a primer was used for reverse-transcription into cDNA. A forward primer mix comprising of consensus sequences for all V-regions and reverse primers for each isotype was used to PCR amplify *Igh* genes. To confirm clonality or for antibody production, *Igk* genes were amplified separately where needed. Afterwards, 5-nucleotide barcodes were introduced by PCR to label Ig-sequences with plate- and well-specific barcodes. The forward and reverse primers contained barcodes to identify the plate and row number, and barcodes to identify the column position, respectively (adapted from Han et al., 2014[49]). A final PCR step was performed to incorporate Illumina paired-end sequencing adapters into single-well amplicons. PCR-products from all plates were pooled together and subsequently cleaned-up using a 0.7x volume ratio of SPRI beads. Sequencing was performed on the Illumina Miseq platform with a 500-cycle Reagent Nano kit v2 as per the manufacturer's instructions. Primer sequences are provided separately.

Analysis of sequencing data

PandaSeq was used to assemble paired-end sequences[50] and processing was performed with the FASTX toolkit. Barcode sequences were used to assign the resulting demultiplexed and collapsed reads to their respective plates and wells. High-count sequences were analyzed for every single cell/well. To determine the V(D)J arrangements and the number of somatic mutations compared to putative germline precursors, Ig heavy chain and Ig light sequences were aligned to the online databases (IMGT[51]; Vbase2[52]). Sequences that shared VH/JH genes, had the same CDR3 lengths, and contained at least 75% CDR3 nucleotide identity were grouped and classified automatically into clonal lineages. Manual curation was performed based on features including V-region SHM patterns and stretches of mismatches at the junctional regions, resulted in further joining of sequences deemed to belong to the same clone, but which fell below 75% CDR3 nucleotide identity. For the few clones in which a rearranged *Igh* gene was not detected, the *Igk* sequence was used to establish clonality. Only cells with productively rearranged *Igh* genes were used for VH mutation analyses. GCtree[53] was used to infer clonal lineage trees, with the unmutated V gene sequence of the V(D)J clonal rearrangement used for outgroup rooting. All sequencing data used in this study can be found in Table S1.

scRNA-seq library preparation and analysis

Total GC B cells were sorted, counted for viability, and immediately subjected to library preparation. We produced gene expression and BCR single-cell libraries using the 10X Chromium Single Cell 5' and V(D)J Enrichment, according to the manufacturer's instructions at the Genomics core of Rockefeller University. The scRNA and BCRseq libraries were sequenced on the Illumina NextSeq500 platform. The sequencing yielded 558 million reads with an average of 194,452 reads per cell using read lengths of R1: 26 bp [16bp cell barcode:10bp Unique Molecular Identifier (UMI)], R2: 57 bp read 2. In addition, single-cell BCR libraries yielded an average sequencing depth of 32,626 reads per cell using read lengths of 151 bp read 1 and 151 bp read 2.

We used hashtag oligonucleotides (HTOs) to pool different biological samples into the same sequencing run. Each sample was stained with one unique HTO (BioLegend, San Diego, USA): HTO1 (M1/42; 30-F11, 155801), HTO2 (M1/42; 30-F11, 155803), HTO3 (M1/42; 30-F11, 155805), HTO4 (M1/42; 30-F11, 155807), and biotinylated anti-CD45.2 (clone 104) followed by streptavidin (405273).

Raw fastq files from our 10X libraries were processed with Cellranger count (v6.2.0). To identify fate-mapped cells from the sequence data, we used a customized mouse genome (mm39) that included the "Ai9" *Rosa26*^{tdTomato} targeting plasmid sequence (Addgene plasmid #22799) as an artificial chromosome with the tdTomato and stop cassette sequences annotated as features to identify fate-mapped and non-fate-mapped cells, respectively. Quality control was performed by removing cells with high (> 10%) mitochondrial UMI content. Cells expressing either zero or more than one hashtag were removed from analyses. Additionally, we removed cells that contained both tdTomato and stop cassette counts. The BCR contig assembly and annotation were performed with the Cellranger vdj workflow from 10X Genomics. BCR clones were characterized by having identical V, (D), J, and CDR3 lengths for the paired *Igh* and *Igk*/*Igl* chains. Clones with a missing chain were considered part of a clonal group when matching 100% of its chain to the clone *Igk* and *Igk*/*Igl* pair.

The matrix of UMI counts was normalized by applying a regression model with a negative binomial distribution, available through the SCTransform function in the Seurat (v41.0) package.[54] The top 3000 variable genes were first used for dimensional reduction by PCA using the scaled data. The first 20 principal components were further used for visualization using the Manifold Approximation and Projection (UMAP) and cell clustering.[54,55] The Wilcoxon rank-sum test was used to detect significant gene markers between groups. P-values were adjusted for multiple testing using the Bonferroni correction method. Genes with adjusted p-values of less than 0.05 were considered downstream analysis. Gene signatures were scored by using the AddModuleScore available by the Seurat package. For the cell cycle signature, gene sets for the S and G2M phases[56] were used to define cycling, and cells that did not score in at least one set were marked as in the G1 phase.

Monoclonal antibody production and binding measurements

mAb Heavy and light chain sequences were synthesized and assembled into Ig production plasmids by Twist Biosciences. 293F cells were transfected with plasmids, and mAbs and Fabs (his-tagged) were purified using protein-G or Ni-NTA (both from Cytiva) affinity chromatography, respectively, as described previously.[25] Bio-layer interferometry (BLI) was performed on an Octet RED96 instrument (ForteBio) to determine affinities of Fabs bound to influenza NP. Briefly, NP (Sino biological) was biotinylated at a 1:1 molar coupling ratio as per the manufacturer's instructions (EZ-link Sulfo NHS-LC-LC-Biotin, Thermo Fisher). NP was loaded onto High Precision Streptavidin (SAX) Biosensors (ForteBio) until binding reached 1 nm. Association was measured by submerging sensors into wells containing Fabs (160 nM – 5 nM in PBS 0.1%BSA/0.02%Tween 20) for 400s. Disassociation was measured by transferring sensors into buffer solution without analyte for 500s. K_D values were determined using the global fit 1:1 binding algorithm provided with the Octet data analysis software. For avidity measurements of invader clones, influenza antigens were biotinylated at a 1:1 molar coupling ratio as per manufacturer's instructions (EZ-link Sulfo NHS-LC-LC-Biotin, Thermo Fisher). For tetramerization, biotinylated antigens were incubated with streptavidin at a 4:1 antigen:streptavidin molar ratio for 30 minutes at room temperature. 10 μg/ml of each mAb was loaded onto anti-human Fab-CH1 2nd Generation (FAB2G) Biosensors (ForteBio). Association was measured by submerging sensors into wells containing 10 μg/ml of monomeric or tetrameric antigen for 120 s. Disassociation was measured by transferring sensors into buffer solution for 120 s.

Preparation of fecal bacteria for ELISA

5 – 10 pellets of feces were collected fresh from B6 mice and immediately placed in Eppendorf tubes on ice. Pellets were mashed with a pestle into ice-cold PBS. The resulting suspension was spun at 500 XG, at 4C for 5 minutes. The supernatant was collected, topped up with PBS, and spun at 4,000 XG for 15 minutes. The pellet was then resuspended in PBS. The fast spin was repeated three more times, after which the resulting pellet was resuspended in 1 ml PBS. The concentration of bacteria was adjusted to reach an OD600 of 0.25. ELISA plates were coated with poly-L-lysine (diluted 1:10 in water) for at least 15 minutes at room temperature and washed 3x with PBS. Plates were coated with an appropriate volume of bacteria overnight at 4C.

ELISA

Antibody binding was determined by ELISA as described previously.[25] For single B cell culture supernatants, total Ig was assayed by coating plates with goat anti-mouse Ig at 1 μg/ml (Southern Biotech). Influenza antigen specificity was screened by coating plates with 5 μg/ml of recombinant PR8 HA, NP, NA, M1, and NS1. Polyreactivity was screened by coating plates with 10 μg/ml of LPS (Sigma, L2637), dsDNA (Sigma), ssDNA, keyhole limpet hemocyanin (KLH) (Sigma, H8283), and 5 μg/ml of human insulin (Sigma, I9278). ssDNA was prepared by incubating dsDNA at 95C for 5 minutes. MDCK cell extracts were coated at 100 μg/ml of total protein, as measured by BCA (Millipore, 71285-3). Coating reagents were incubated in PBS at 4°C overnight. Wells were blocked with 2% BSA for 2 h at room temperature after 3 washes with PBS with 0.05% Tween20 (PBS-T). mAbs were diluted to the specified concentrations in PBS supplemented with 1% BSA and incubated in the wells for 2 h. For Ig from single GC B cell cultures, 30 μl of supernant was added to each well. Wells were washed 4 times with PBS-T before incubation with anti-human IgG conjugated to horse radish peroxidase (HRP) for 1 hr. ELISAs were developed with TMB (slow kinetic form, Sigma). Absorbance at 450 nm was measured on a Fisher Scientific accuSkan FC plate reader.

QUANTIFICATION AND STATISTICAL ANALYSIS

Statistical tests used to compare conditions are indicated in figure legends. Statistical analysis was carried out using GrahPad Prism v.8. Flow cytometry analysis was carried out using FlowJo v.10 software. Graphs were plotted using Prism v.8 and GCtree, and edited for appearance using Adobe Illustrator CS. Statistical details of experiments are provided in the results, figures and corresponding figure legends.

CellPress

Supplemental figures

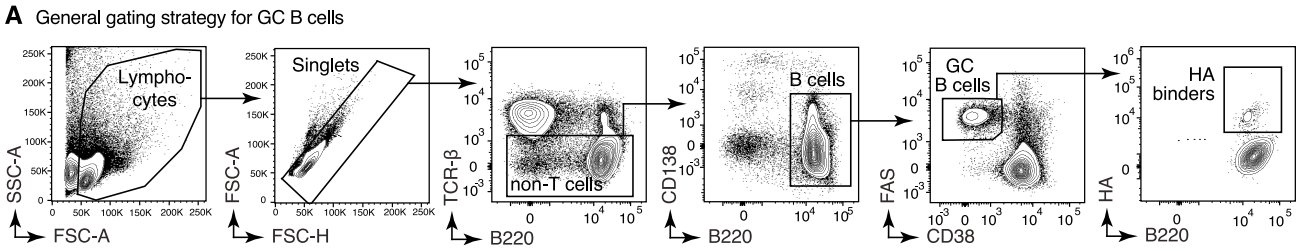

Figure S1. Standard gating strategy on germinal center B cells, related to Figure 1

Gating strategy for GC B cells used in Figure 1 and subsequent figures. Plots are from a mediastinal lymph node of a wild-type C57BL/6 mouse, 12 weeks post-infection with PR8 influenza.

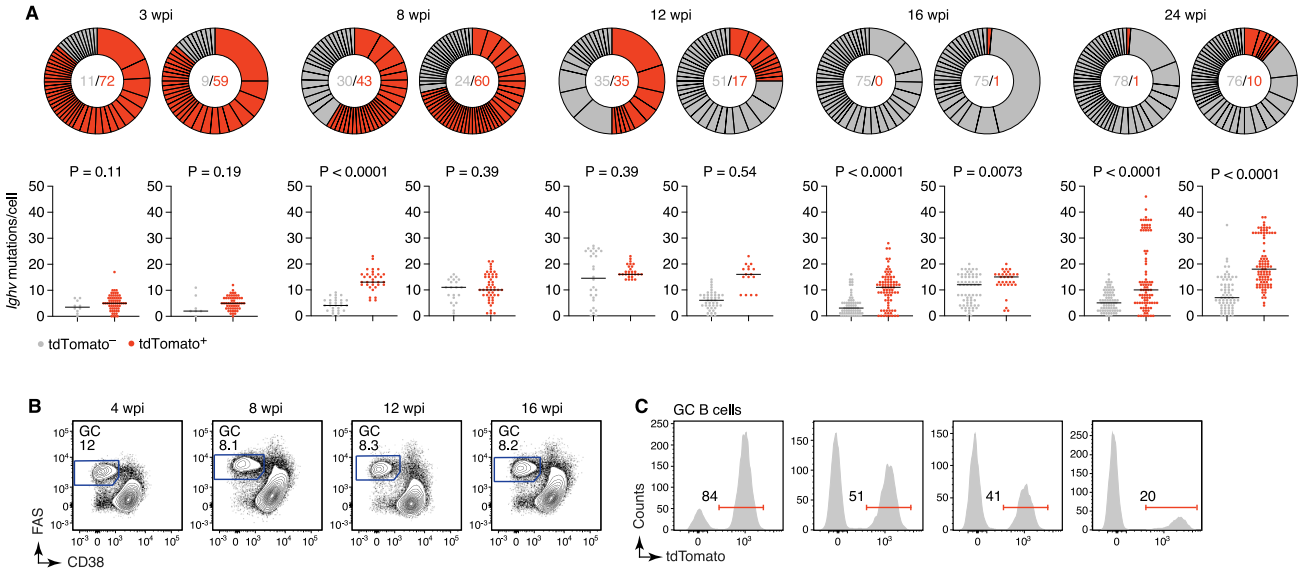

Figure S2. Replacement of founder clones over time in influenza and SARS-CoV-2-primed LLGCs. related to Figure 2

(A) Additional S1pr2-Tomato mice analyzed in Figures 2F and 2G. Pie charts show clonal distribution of tdTomato$^+$ founder (red) and tdTomato invader (gray) B cells sorted from GCs at different time points after influenza infection. Each slice represents one clone (defined as B cells with the same *Igh* VDJ rearrangement). Gray and red numbers in the center of the pie charts denote how many invaders and founders were sequenced, respectively, when GC B cell samples were sorted in an unbiased manner (thus the zero fate-mapped cells in some pie charts). Additional plates of rare fate-mapped GC B cells were sorted for late time points (16 and 24 wpi).

(B and C) Representative flow cytometry plots from data presented in Figures 2K and 2L, showing frequency of GC B cells (FAS$^+$CD38^{low}) among total B cells (B220$^+$) (B) and frequency of fate-mapped B cells among all GC B cells (C) in the mLN of tamoxifen-pulsed S1pr2-Tomato mice at different time points after SARS-CoV-2 infection.

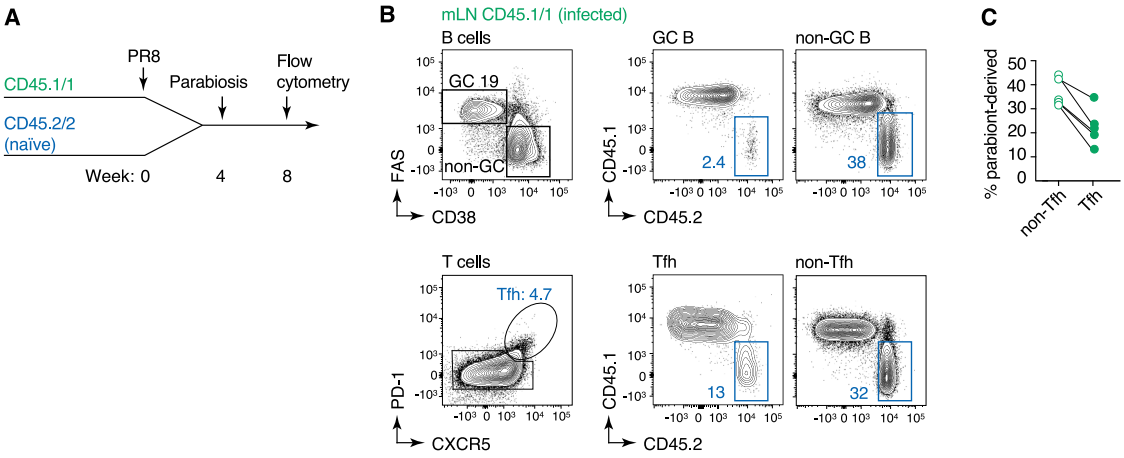

Figure S3. Tfh exchange pattern in long-lived germinal centers, related to Figure 2

(A) Experimental setup.

(B and C) 8 weeks after infection (4 weeks after surgery), pairs were sacrificed and the frequency of Tfh/GC B cells (B), alongside the chimerism in the B cell (GC and non-GC B) and T cell compartments (Tfh and non-Tfh), was analyzed in the infected mouse (CD45.1/1), and the degree of chimerism in Tfh cells is shown as a graph, in multiple pairs analyzed (C).

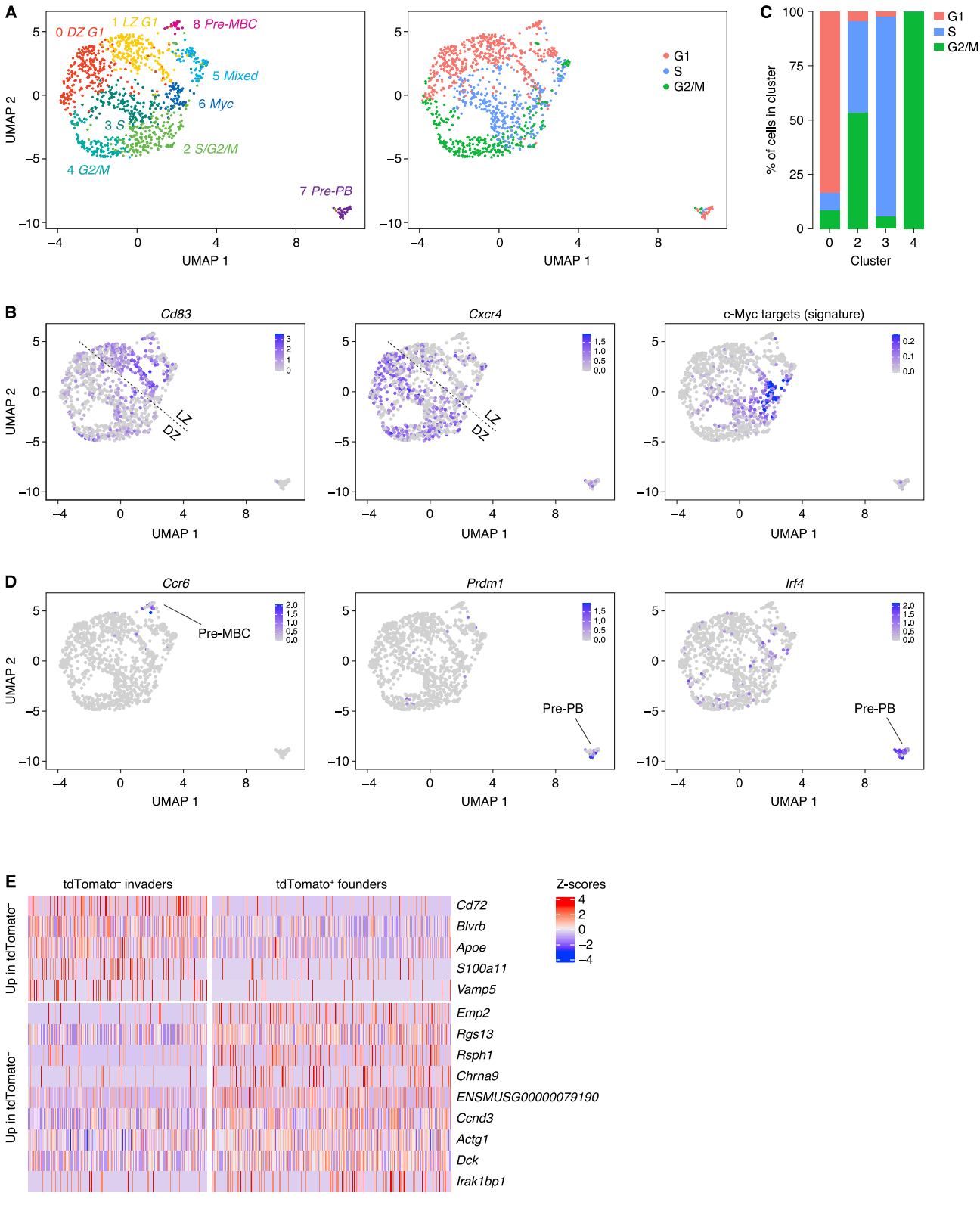

Figure S4. Clonal and transcriptional characteristics of founder and invader B cells, related to Figure 4

(A–D) Biological interpretation of the clusters emerging from scRNA-seq data. We chose a resolution at which GC B cells could be resolved into 9 clusters defined by GC zone, cell cycle stage (as assigned by transcriptional signature), and post-GC fates (A). Left, UMAP clustering (reproduced from Figure 4I); right, inferred

(legend continued on next page)

cell-cycle stage. (B) LZ cells expressed higher levels of *Cd83* and were divided into clusters 1 (*LZ G1*) and 6 (*Myc*), corresponding to B cells prior to and following positive selection, respectively. DZ cells expressed higher levels of *Cxcr4*. UMAP plots show expression of individual genes (*Cd83*, *Cxcr4*) and of a compound signature of c-Myc targets (MYC1).[57] (C) DZ B cells were divided into 4 clusters primarily driven by cell cycle stage. (D) Clusters 7 and 8 were enriched in cells expressing *Ccr6* (cluster 7) and *Prdm1* and *Irf4* (cluster 8), likely representing GC B cells en route to export as memory B cells and plasmablasts, respectively. Cluster 5 contained a mixture of cells from different zones and in different stages of cell cycle. Lower detection of ribosomal protein-encoding mRNAs in this cluster (not shown) is suggestive of a technical artifact of the method in this cluster.
(E) Heatmap showing genes differentially expressed between tdTomato^{+} founder and tdTomato^{-} invader B cells at 8 wpi.

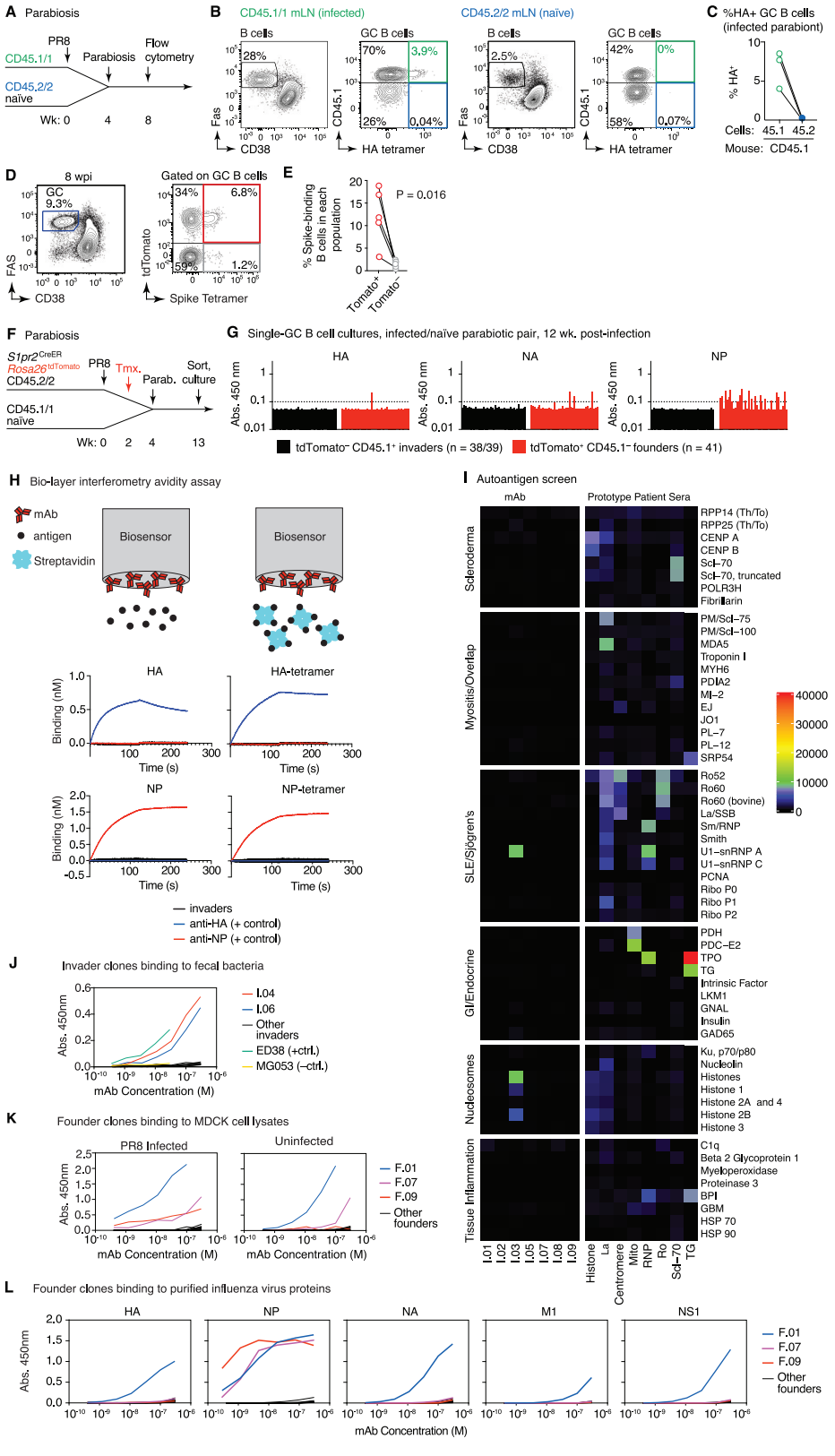

(legend on next page)

Figure S5. Binding characteristics of invader and founder B cells in LLGCs, related to Figures 5 and 6

(A) Experimental setup.

(B) Flow cytometry plots showing the frequency of endogenous and parabiont-derived GC B cells that bind HA in the naive (left) and infected (right) mLN.

(C) Quantification of data as in (B).

(D) Representative flow cytometry plots showing binding of fate-mapped and non-fate-mapped GC B cells to SARS-CoV-2 Spike protein at 8 wpi.

(E) Quantification of data as in (D). Each pair of symbols represents one mouse. p value is for paired t test.

(F) Experimental setup. An S1pr2-Tomato, CD45.2 mouse is infected with influenza, GC B cells are fate-mapped at 2 wpi, and this mouse is joined parabiotically to a naive CD45.1 partner at 4 wpi. Cells from the infected mLN are then sorted for single-B cell culture.

(G) Binding of founder ($tdTomato^{+}CD45.2^{+}$) and invader ($tdTomato^{-}CD45.1^{+}$) GC B cells to influenza HA, NA, and NP antigens 13 wpi. GC B cells were sorted from the mLN of the S1pr2-Tomato parabiont into 96-well plates for single-cell (Nojima) culture, and IgG^{+} supernatants were assayed against influenza antigens by ELISA. Each bar represents one IgG^{+} culture. Data are from one mouse.

(H) Bio-layer interferometry avidity assay to assess binding of invader mAbs to HA and NP (mid and lower graphs). Antibody valency is increased by loading mAbs onto the biosensor (upper illustration, left). Antigen valency is increased by tetramerization with streptavidin (upper illustration, right). Anti-HA and anti-NP mAbs are included as positive and negative controls.

(I) Heatmap showing reactivity of mAbs cloned from invader clones against common autoantigens grouped based on disease, along with DNA-associated antigens and antigens associated with tissue inflammation or stress response (left). Prototype patient sera are shown as positive controls (right).

(J) ELISA titration curves for mAbs cloned from invader clones binding to fecal bacteria from B6 mice. mAbs Ed38 and MG053 were included as positive and negative controls, respectively.

(K) ELISA curves of mAbs cloned from founder clones binding to uninfected and PR8-infected MDCK cell lysates.

(L) ELISA curves for founder clone mAbs binding to a panel of influenza antigens (HA, NP, NA, M1 and NS1).

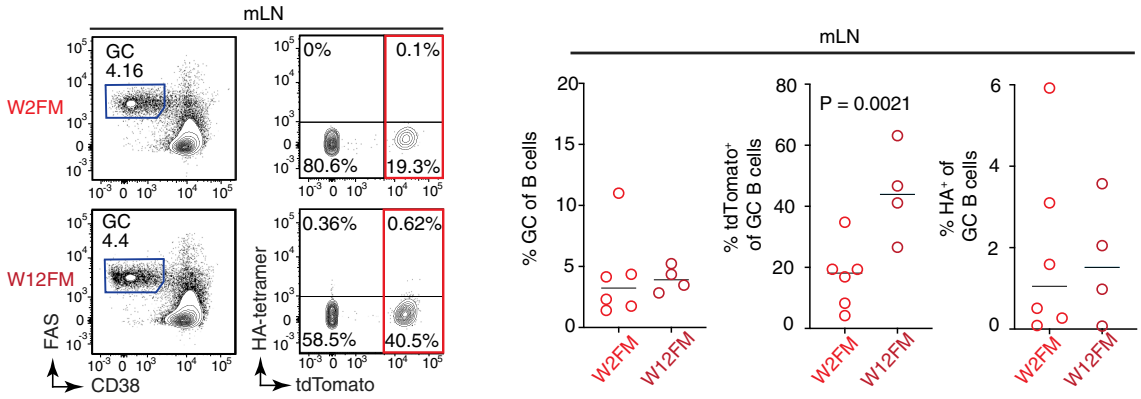

Figure S6. Frequency of total GC and HA-specific B cells in mice fate-mapped at week 2 or 12 after infection, related to Figure 7

Representative flow cytometry plots showing frequency of GC B cells (FAS^+CD38^{low}) among total B cells ($B220^+$) and frequency of fate-mapped and HA-binding B cells among all GC B cells in the mLN of tamoxifen-pulsed S1pr2-Tomato mice (as depicted in Figure 7A). Graphs on the right show pooled data from 2 independent experiments. Each symbol is one mouse, the line represents the mean.